

# CM<sup>2</sup> MAGAZINE



第 82 期



南方科技大学海洋磁学中心主编

<http://cm2.sustech.edu.cn/>

## 创刊词

海洋是生命的摇篮，是文明的纽带。地球上最早的生命诞生于海洋，海洋里的生命最终进化成了人类，人类的文化融合又通过海洋得以实现。人因海而兴。

人类对海洋的探索从未停止。从远古时代美丽的神话传说，到麦哲伦的全球航行，再到现代对大洋的科学钻探计划，海洋逐渐从人类敬畏崇拜幻想的精神寄托演变成可以开发利用与科学研究的客观存在。其中，上个世纪与太空探索同步发展的大洋科学钻探计划将人类对海洋的认知推向了崭新的纬度：深海（deep sea）与深时（deep time）。大洋钻探计划让人类知道，奔流不息的大海之下，埋藏的却是亿万年的地球历史。它们记录了地球板块的运动，从而使板块构造学说得到证实；它们记录了地球环境的演变，从而让古海洋学方兴未艾。

在探索海洋的悠久历史中，从大航海时代的导航，到大洋钻探计划中不可或缺的磁性地层学，磁学发挥了不可替代的作用。这不是偶然，因为从微观到宏观，磁性是最基本的物理属性之一，可以说，万物皆有磁性。基于课题组的学科背景和对海洋的理解，我们对海洋的探索以磁学为主要手段，海洋磁学中心因此而生。

海洋磁学中心，简称  $CM^2$ ，一为其全名“Centre for Marine Magnetism”的缩写，另者恰与爱因斯坦著名的质能方程  $E = MC^2$  对称，借以表达我们对科学巨匠的敬仰和对科学的不懈追求。

然而科学从来不是单打独斗的产物。我们以磁学为研究海洋的主攻利器，但绝不仅限于磁学。凡与磁学相关的领域均是我们关注的重点。为了跟踪反映国内外地球科学特别是与磁学有关的地球科学领域的最新研究进展，海洋磁学中心特地主办  $CM^2$  Magazine，以期与各位地球科学工作者相互交流学习、合作共进！

“海洋孕育了生命，联通了世界，促进了发展”。21世纪是海洋科学的时代，由陆向海，让我们携手迈进中国海洋科学的黄金时代。

# 目录

1. 冰期-间冰期的转移支配着热带印-太平洋晚更新世水文变化 .....	4
2. 人类过去三十万年从非洲出走的气候窗口 .....	8
3. 喜马拉雅碰撞如何源于俯冲 .....	11
4. 过去 1.36 Ma 地中海森林残遗种保护区动态对冰期-间冰期旋回强度的响应 .....	14
5. SINOPROBE 剖面揭示的华南西北部安第斯型弧后前陆盆地系统 .....	18
6. 海洋沉积物低温磁性特征-磁小体, 超顺磁, 磁赤铁矿化定量分析: 以地中海东部为例 .....	21
7. 伴随沉积放大效应的南大洋过程造成冰期碳循环变化 .....	25
8. 巴拉望中南部古近系同裂谷沉积物的地层特征和物源:对华南陆缘的古地理重建意义	28
9. 来自中国中部重庆的 40000 年的植被, 环境和气候变化记录 .....	30
10. 马达加斯加西北部石笋记录揭示了 8.2 ka 事件的时间和特征 .....	33
11. 古强度结果偏差校正 (BiCEP): 一个提高的方法对于获得古强度结果 .....	38
12. 间冰期结束时, 由辐射量引发的大西洋环流突然减弱 .....	41

# 1. 冰期-间冰期的转移支配着热带印-太平洋晚更新世水文变化



翻译人：仲义 zhongyi@sustech.edu.cn

Windler, G., Tierney, J E., Anchukaitis, K J., et al. **Glacial-Interglacial shifts dominate tropical Indo-Pacific hydroclimate during the late Pleistocene** [J] *Geophysical Research Letters*, 48(15), e2021GL093339.

<https://doi.org/10.1029/2021GL093339>

**摘要：**晚更新世以来的热带地区降水和大气环流的气候驱动因素还存在争议。一些研究认为热带沉积主要受控于岁差周期（23-19 kyr），同时也有人强调冰盖中冰期-间冰期（100kyr）的冰盖和海平面变化占主导。本文中，作者利用奇异谱分析的方法从印度-太平洋暖池（IPWP）和亚洲季风区域的代用指标中分离出主要的振荡模态，重新研究了轨道周期对热带到亚热带沉积同位素特征。研究人员发现 IPWP、孟加拉湾和南海主要是由冰期-间冰期的 100kyr 周期模式控制，而中国东部明显呈现出岁差周期，表明降水同位素结果在亚洲大陆中纬度地区与 IPWP、印度和东亚季风区响应了不同受控机制。本项研究证明冰期旋回而非区域性光照是驱动晚更新世印-太平洋水文循环的主要因素。

**ABSTRACT:** The climatic drivers of tropical rainfall and atmospheric circulation in the late Pleistocene are still debated. Some studies suggest that tropical precipitation primarily responded to precession (23–19 ky cycle), whereas others propose that glacial-interglacial (100 ky) changes in ice sheets and sea level dominate. Here, we reexamine orbital influences on tropical-to-subtropical precipitation isotopes using singular spectrum analysis to isolate leading oscillatory modes from proxy records across the IndoPacific Warm Pool (IPWP) and Asian monsoon domain. We find that the IPWP, Bay of Bengal, and South China Sea are dominated by the 100 ky glacial-interglacial mode of variability, whereas eastern China clearly follows precession, suggesting that precipitation isotopes over the mid-latitude Asian continent respond to different mechanisms than those in the IPWP or Indian and East Asian monsoon regions. This study demonstrates that glacial cycles, rather than changes in local insolation, are the dominant drivers of Pleistocene IPWP hydroclimate.

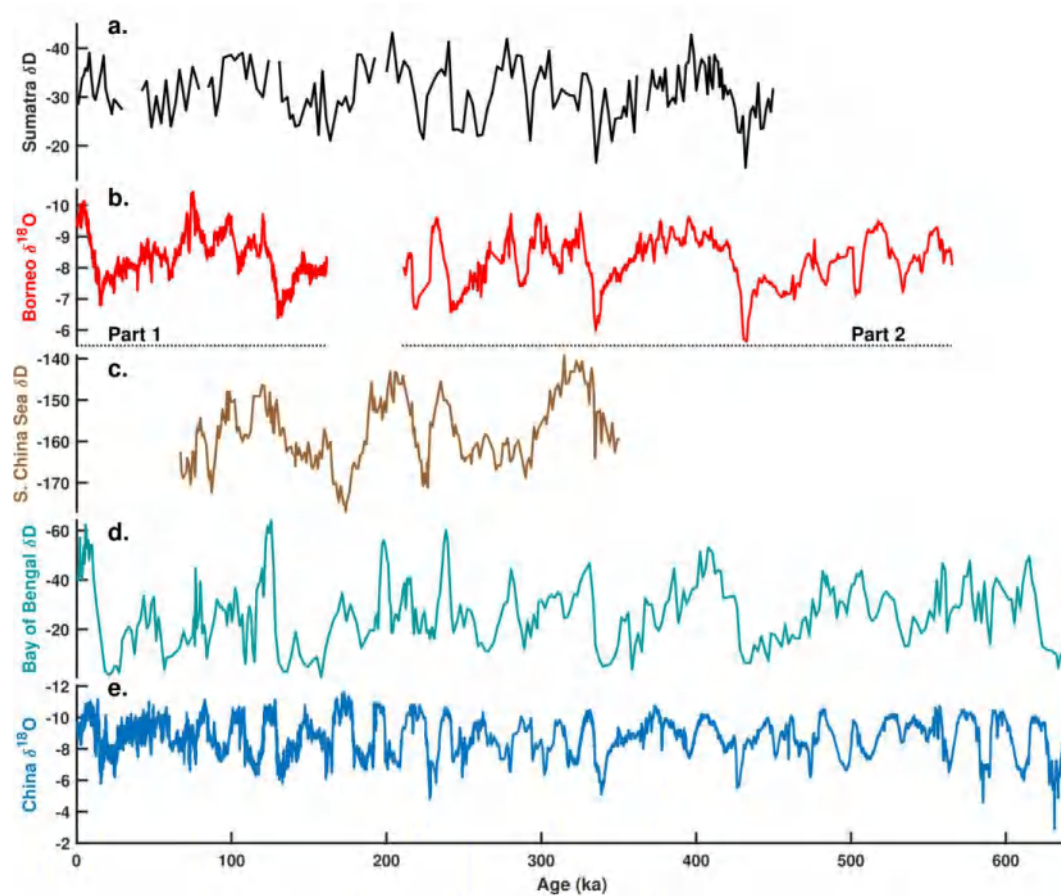


**Figure 1.** Paleoclimate data used in this study. (a) Sumatra  $\delta D_{precip}$  (Windler et al., 2020). (b) Borneo1  $\delta^{18}O_{speleo}$  (Carolin et al., 2016) and Borneo2 (Meckler et al., 2012). (c) South China Sea  $\delta D_{wax}$  (Thomas et al., 2014). (d) Bay of Bengal  $\delta D_{precip}$  (McGrath et al., 2021). (e) Composite China  $\delta^{18}O_{speleo}$  (Cheng et al., 2016). All y-axes are reversed except panel (c).

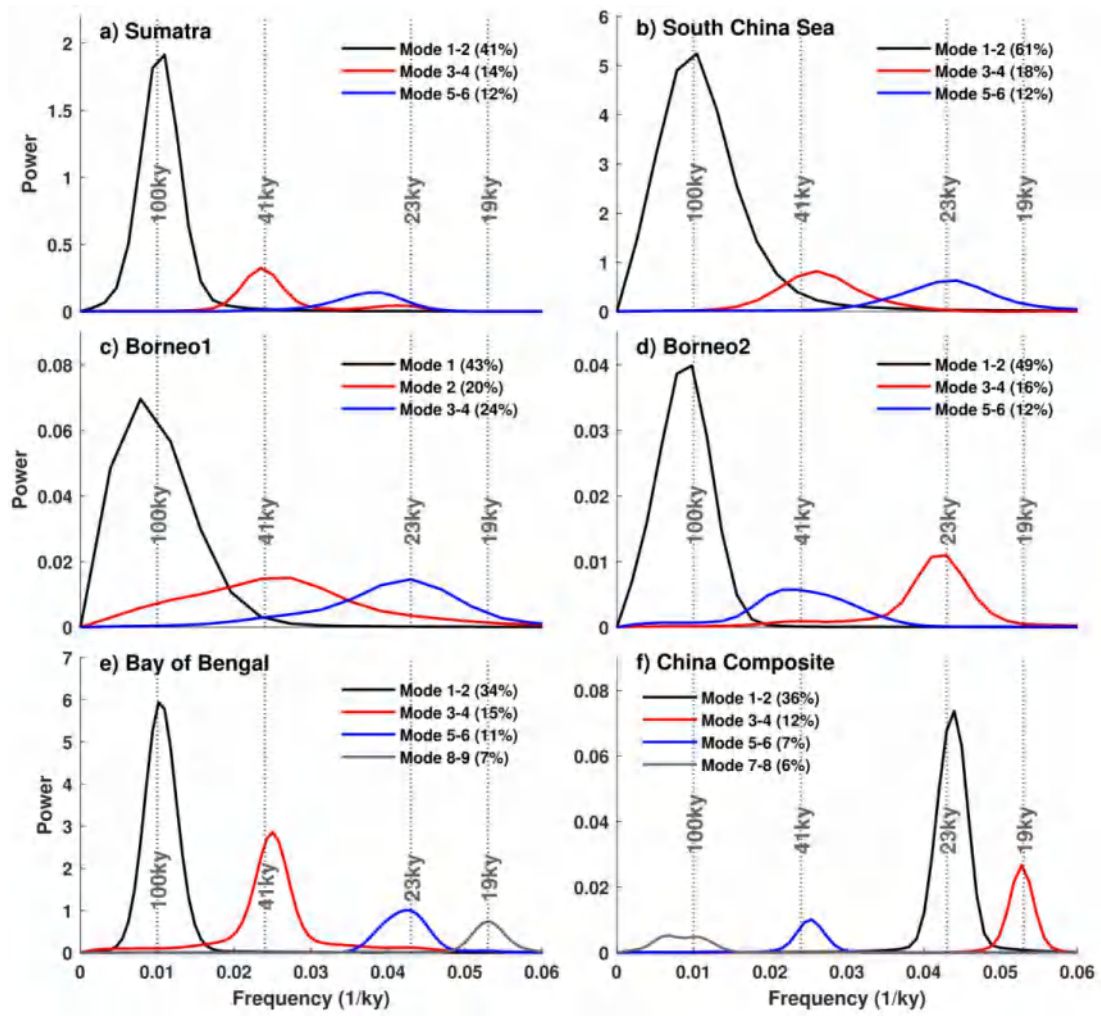


**Figure 2.** Smoothed periodograms of leading modes for (a) Sumatra, (b) South China Sea, (c and d) Borneo, (e) Bay of Bengal, and (f) China. Modes that are in quadrature are listed as pairs. Explained variance for each mode are listed in each panel.

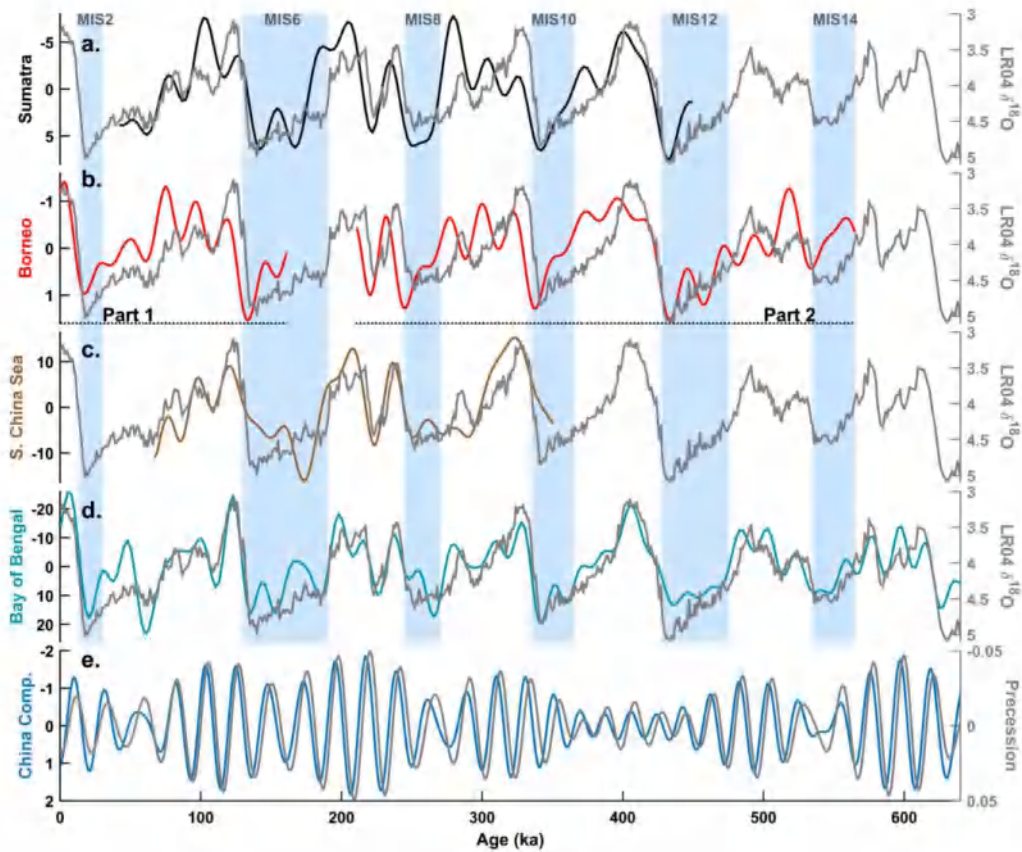


**Figure 3.** Reconstructed components (RCs) of meaningful modes of variability for (a) Sumatra: modes 1–6, (b) Borneo: modes 1–4 from Borneo1 and modes 1–6 from Borneo2, (c) South China Sea: modes 1–6, (d) Bay of Bengal: modes 1–9 excluding mode 7, and (e) China: modes 1–4. RCs are plotted against either the LR04 benthic stack (Lisiecki & Raymo, 2005) (panels a–d), or precession (Laskar et al., 2004) (panel e). All y-axes are reversed except panel (c). Glacial marine isotope stages are highlighted in blue.

## 2. 人类过去三十万年从非洲出走的气候窗口



翻译人: 蒋晓东 [jiangxd@sustech.edu.cn](mailto:jiangxd@sustech.edu.cn)

*Beyer R M, Krapp M, Eriksson A, et al. Climatic windows for human migration out of Africa in the past 300,000 years [J]. Nature Communications, 2021, 12, 4889.*

<https://doi.org/10.1038/s41467-021-24779-1>

**摘要:** 虽然人类来自非洲的观点已被广泛认同,但他们迁徙到欧亚大陆的时间和路径争议非常激烈,这主要是因为缺乏化石和合适的古人类 DNA 记录。本研究通过高分辨率古气候重建,去估算降雨影响下人类过去 30 万年离开非洲大陆的困难性。基于分析结果并联合人类学和生态学驱动,我们估算狩猎-采集存活下来所需降雨的最低水平,重建了气候驱动下人类何时沿着怎样的地理路径从非洲出走的可能性。我们估算的时间和路径与欧亚大陆潜在的联系,正好适配人类从非洲出走在考古学和基因分析上的证据。这些结果指出了气候变化在现今人类扩散中的关键角色。

**ABSTRACT:** Whilst an African origin of modern humans is well established, the timings and routes of their expansions into Eurasia are the subject of heated debate, due to the scarcity of fossils and the lack of suitably old ancient DNA. Here, we use high-resolution palaeoclimate reconstructions to estimate how difficult it would have been for humans in terms of rainfall availability to leave the African continent in the past 300k years. We then combine these results with an anthropologically and ecologically motivated estimate of the minimum level of rainfall required by hunter-gatherers to survive, allowing us to reconstruct when, and along which geographic paths, expansions out of Africa would have been climatically feasible. The estimated timings and routes of potential contact with Eurasia are compatible with archaeological and genetic evidence of human expansions out of Africa, highlighting the key role of palaeoclimate variability for modern human dispersals.

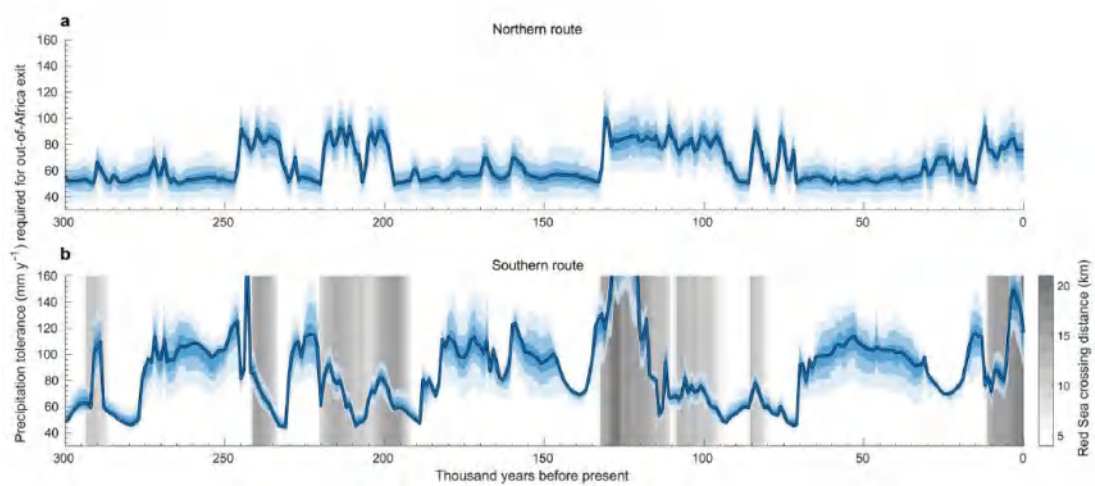


**Figure 1.** Tolerance to low precipitation that would have been required for *Homo sapiens* to leave the African continent in the past 300k years. Blue lines represent minimum precipitation levels for which a connected path between Africa and Eurasia along the a northern b southern route existed, i.e. the minimum levels that humans would have had to withstand for a successful exit along these routes, based on climatological normals at 1k-year time steps (Methods). Thus, higher values correspond to a more favourable climate along the routes. Blue shades represent the 10–90th percentiles of the minimum precipitation tolerance required for a successful exit based on decadal scale climate (Methods). Grey shades in b represent the minimum distance needed to continuously cover on water to reach the Arabian Peninsula from Africa.

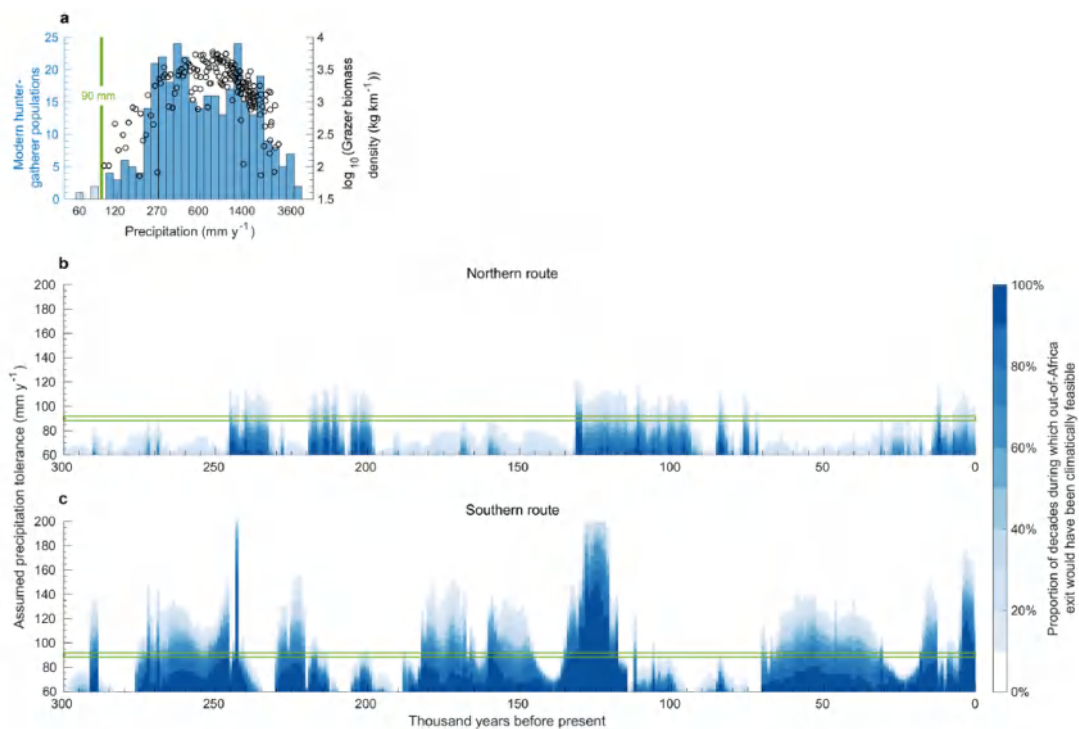


**Figure 2.** Climatic Windows of opportunity out of Africa. a Distribution of modern hunter-gatherer populations (histograms) under different precipitation levels and in relation to grazer biomass density<sup>39</sup> (black markers). Transparent bins correspond to populations located in close vicinity of a water source, which are not considered to be constrained by precipitation. b, c Percentage of decades within a given millennium (x-axis) during which a connected path between Africa and Eurasia along the b northern and c southern route existed for a given hunter-gatherer tolerance to low precipitation (y-axis). The green band represents our empirically estimated threshold of 90  $\text{mm y}^{-1}$ .

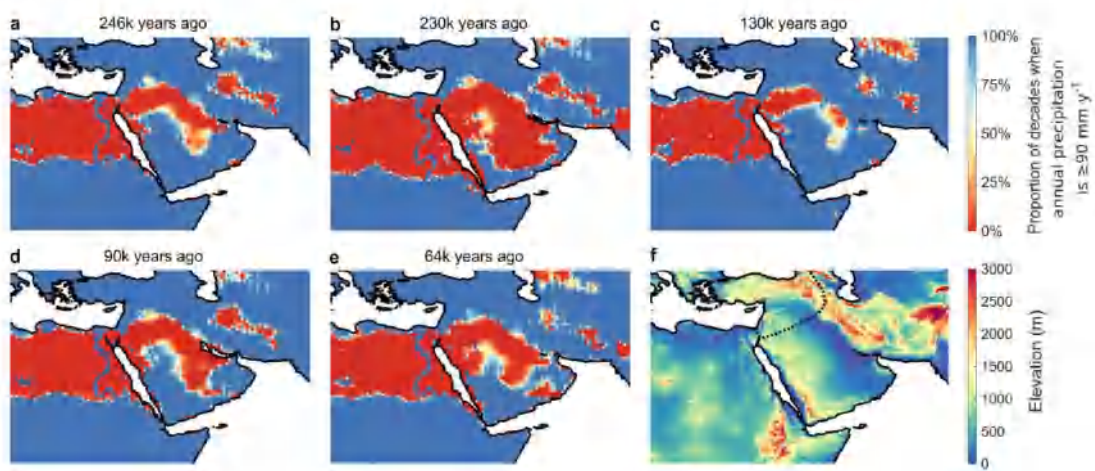


**Figure 3.** Environmental conditions in Northwest Africa and on the Arabian Peninsula. Maps (a–e) illustrate reconstructed precipitation conditions at different points in time. Dark blue areas are estimated to have been sufficiently wet to support human persistence during most of the millennium shown, red areas were likely long-term unsuitable for human persistence, and orange, yellow, and light blue areas were inhabitable during intermittent periods. a, c, d, e correspond to key possible exit timings based on archaeological or genetic evidence while b exemplifies challenging conditions between windows of opportunity. The dotted line in the elevation map (f) represents the reconstructed Neanderthal range at 120k years ago<sup>2</sup>. Inhabitability maps for each millennium, and the analogous, very similar, maps based on Köppen aridity are shown in Supplementary Movie 2.

### 3. 喜马拉雅碰撞如何源于俯冲



翻译人: 冯婉仪 fengwy@sustech.edu.cn

Soret M, Larson K P, Cottle J, et al. *How Himalayan collision stems from subduction* [J]. *Geology*, 2021, 49: 894-898.

<https://doi.org/10.1130/G48803.1>

**摘要:** 在板块边缘, 由大陆俯冲向大陆碰撞转换的发生机制和过程尚不清楚。记录这一转换过程的岩石很少, 要么没有出露, 要么在随后的事件中被抹掉。我们研究了西喜马拉雅造山楔的巴罗变质岩的构造-变质史。研究表明, 这些岩石在 $\leq 47$  Ma 至  $39 \pm 1$  Ma 期间埋藏于角闪岩相的条件下, 与超高压榴辉岩的形成 (46 Ma) 和局部折返 (45 - 40 Ma) 是同步的。这一关联表明, 在大陆俯冲的过程中, 板块的汇聚是由深部造山楔的发育导致的, 而这些深部造山楔是通过大陆物质 (包括部分出露的榴辉岩) 的连续底侵形成的, 这可能是对板块间耦合增加的响应。这一过程导致了俯冲界面通过平流和/或传导热传递加热 (从 $\sim 7$  °C/km 加热至  $20$  °C/km)。造山楔从 38 Ma 开始迅速冷却, 与前陆盆地的形成同时发生, 这被解释为厚印度地壳的隆起压陷的结果。

**ABSTRACT:** The mechanisms and processes active during the transition from continental subduction to continental collision at the plate interface are largely unknown. Rock records of this transition are scarce, either not exposed or obliterated during subsequent events. We examine the tectono-metamorphic history of Barrovian metamorphic rocks from the western Himalayan orogenic wedge. We demonstrate that these rocks were buried to amphibolite-facies conditions from  $\leq 47$  Ma to  $39 \pm 1$  Ma, synchronously with the formation (46 Ma) and partial exhumation (45–40 Ma) of the ultrahigh-pressure eclogites. This association indicates that convergence during continental subduction was accommodated via development of a deep orogenic wedge built through successive underplating of continental material, including the partially exhumed eclogites, likely in response to an increase in interplate coupling. This process resulted in the heating of the subduction interface (from  $\sim 7$  to  $\sim 20$  °C/km) through advective and/or conductive heat transfer. Rapid cooling of the wedge from 38 Ma, coeval with the formation of a

foreland basin, are interpreted to result from indentation of a promontory of thick Indian crust.

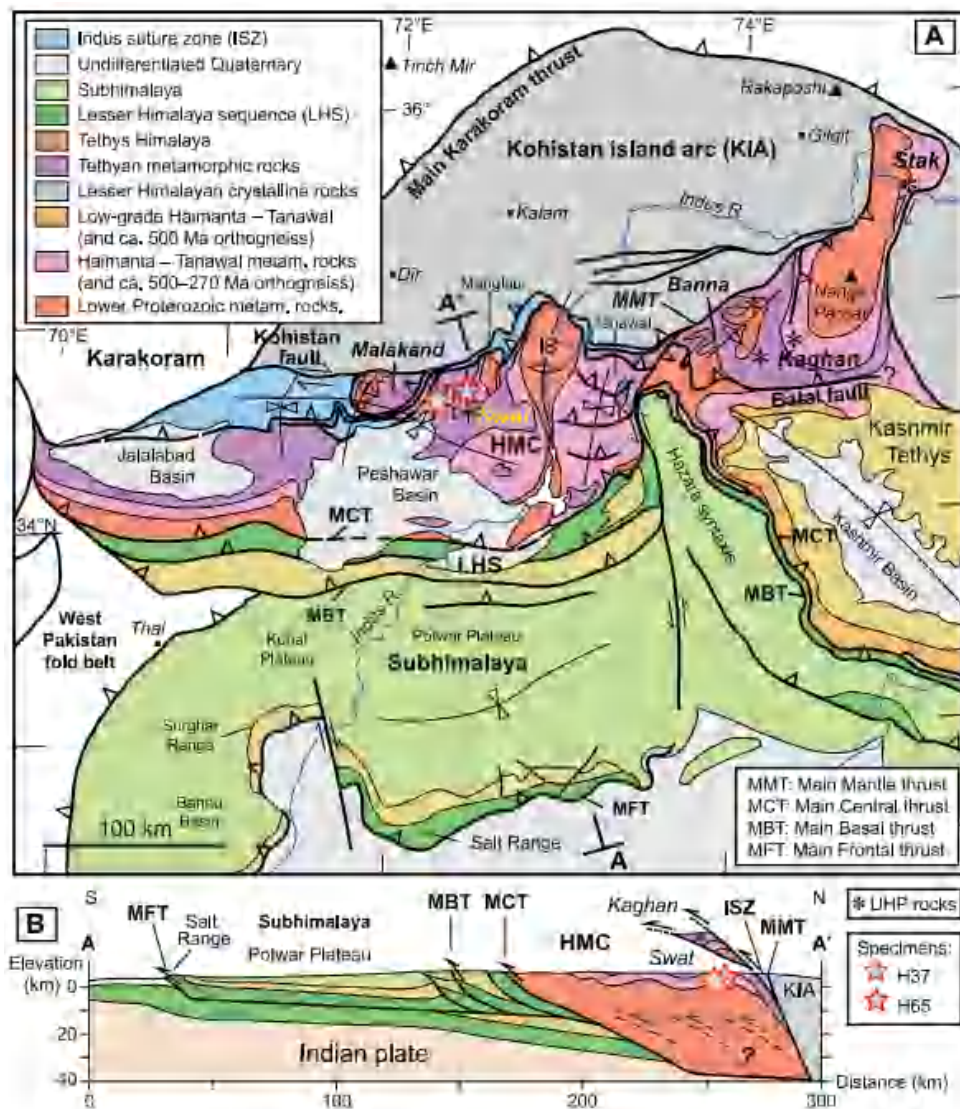
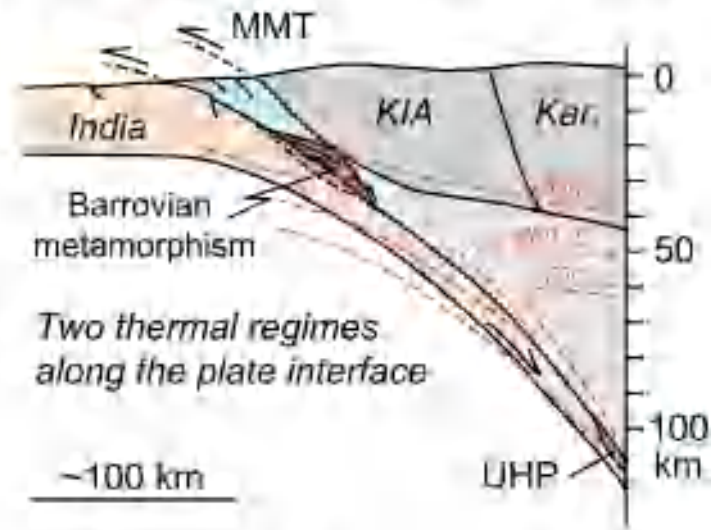
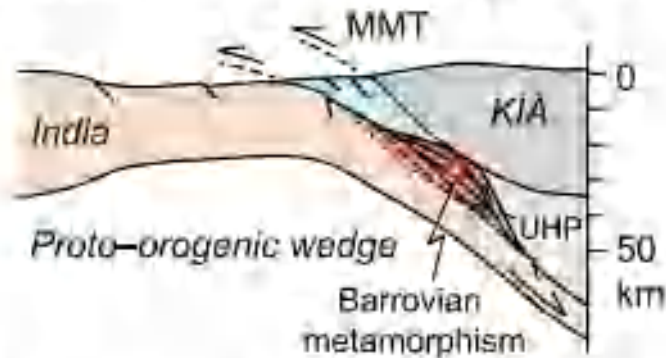


**Figure 1.** (A) Geological map of the western Himalaya. Stars are sampling locations. (B) Present-day section across collisional wedge. The out-of-section thrust sheet outlines the relative structural position of ultrahigh-pressure (UHP) rocks in the Nanga Parbat region (Pakistan). Figures are modified after DiPietro and Pogue (2004). HMC—Himalayan metamorphic core; metam.—metamorphic.

**1a) Continental subduction (50–45 Ma)**



**1b) Continental subduction (45–40 Ma)**



**2) Collision initiation (35–30 Ma)**

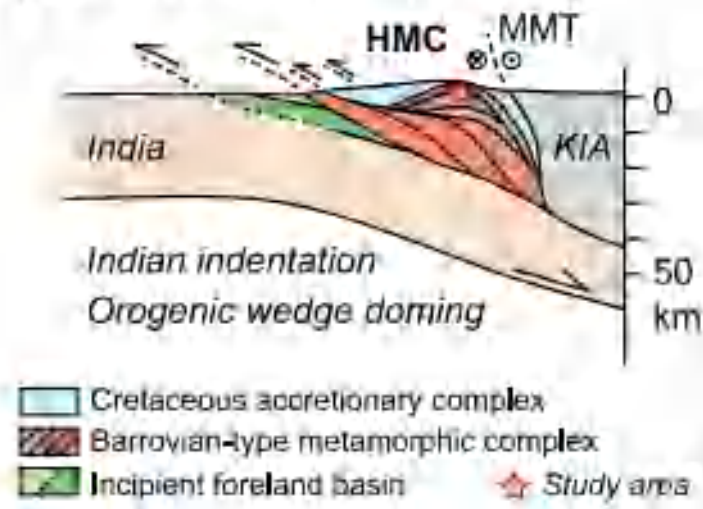


**Figure 2.** Three-stage tectonic model for the transition between subduction and collision dynamics in the western Himalaya. Kar.—Karakoram; UHP—ultrahigh pressure; see Figure 1 for other abbreviations.

## 4. 过去 1.36 Ma 地中海森林残遗种保护区动态对冰期-间冰期旋回强度的响应



翻译人:李园洁 liyj3@sustech.edu.cn

*Donders T, Panagiotopoulos K, Koutsodendris A, et al. 1.36 million years of Mediterranean forest refugium dynamics in response to glacial–interglacial cycle strength[J]. Proceedings of the National Academy of Sciences, 2021, 118(34).*

<https://doi.org/10.1073/pnas.2026111118>

**摘要:** 奥赫里德湖沉积物记录代表着欧洲最长的湖泊资料, 持续到过去 1.36 Ma。我们基于 DEEP 岩芯的孢粉分析重建植被历史, 揭示出冰期-间冰期 (G-IG) 旋回中植被覆盖和森林多样性的变化以及盆地早期演化。最早的湖泊相, 植物组成明显不同, 孑遗树类群多, 草本植物少。之后~1.2 Ma 一个永久性的草原草本植物群落的建立, 表明对湿度可利用性和温度变化的阈值响应和盆地形态的逐渐调整。早-中更新世过渡期 G-IG 旋回的一个变化反映在植被重组的记录中, 从倾斜率周期到偏心率周期旋回。根据树类群丰富度的定量分析, 树木的多样性的第一个大尺度降低发生在~0.94 Ma。之后树木丰富度的变化很大程度受到 G-IG 旋回的幅度和持续时间的驱动。在干燥草本植物群落丰富时期, 树木丰富度显著下降, 表明干旱影响了树木种群的生存。全球气候和区域植被变化之间的长期遗留效应的评估, 揭示了冷的间冰期条件对后续冰期植被组成和多样性的重要影响。这种效应与高纬度观测的相反-冰期的强度控制着之后间冰期植被, 证明了奥赫里德湖流域为喜温和温带植物提供了残遗种保护区。

**ABSTRACT:** The sediment record from Lake Ohrid (Southwestern Balkans) represents the longest continuous lake archive in Europe, extending back to 1.36 Ma. We reconstruct the vegetation history based on pollen analysis of the DEEP core to reveal changes in vegetation cover and forest diversity during glacial-interglacial (G-IG) cycles and early basin development. The earliest lake phase saw a significantly different composition rich in relict tree taxa and few herbs. Subsequent establishment of a permanent steppic herb association around 1.2 Ma implies a threshold response to changes in moisture availability and temperature and gradual adjustment of the basin morphology. A change

in the character of G-IG cycles during the Early - Middle Pleistocene Transition is reflected in the record by reorganization of the vegetation from obliquity- to eccentricity-paced cycles. Based on a quantitative analysis of tree taxa richness, the first large-scale decline in tree diversity occurred around 0.94 Ma. Subsequent variations in tree richness were largely driven by the amplitude and duration of G-IG cycles. Significant tree richness declines occurred in periods with abundant dry herb associations, pointing to aridity affecting tree population survival. Assessment of long-term legacy effects between global climate and regional vegetation change reveals a significant influence of cool interglacial conditions on subsequent glacial vegetation composition and diversity. This effect is contrary to observations at high latitudes, where glacial intensity is known to control subsequent interglacial vegetation, and the evidence demonstrates that the Lake Ohrid catchment functioned as a refugium for both thermophilous and temperate tree species.

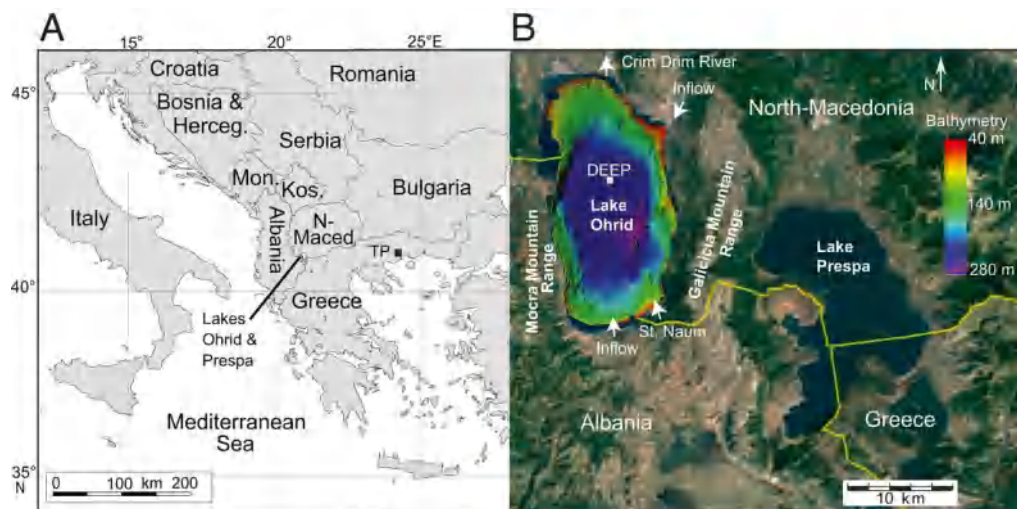


**Figure 1.** (A) Location of LO and TP on the Balkan Peninsula. (B) Local setting around LO, bathymetry (81), and DEEP coring site (adapted from ref. 32).

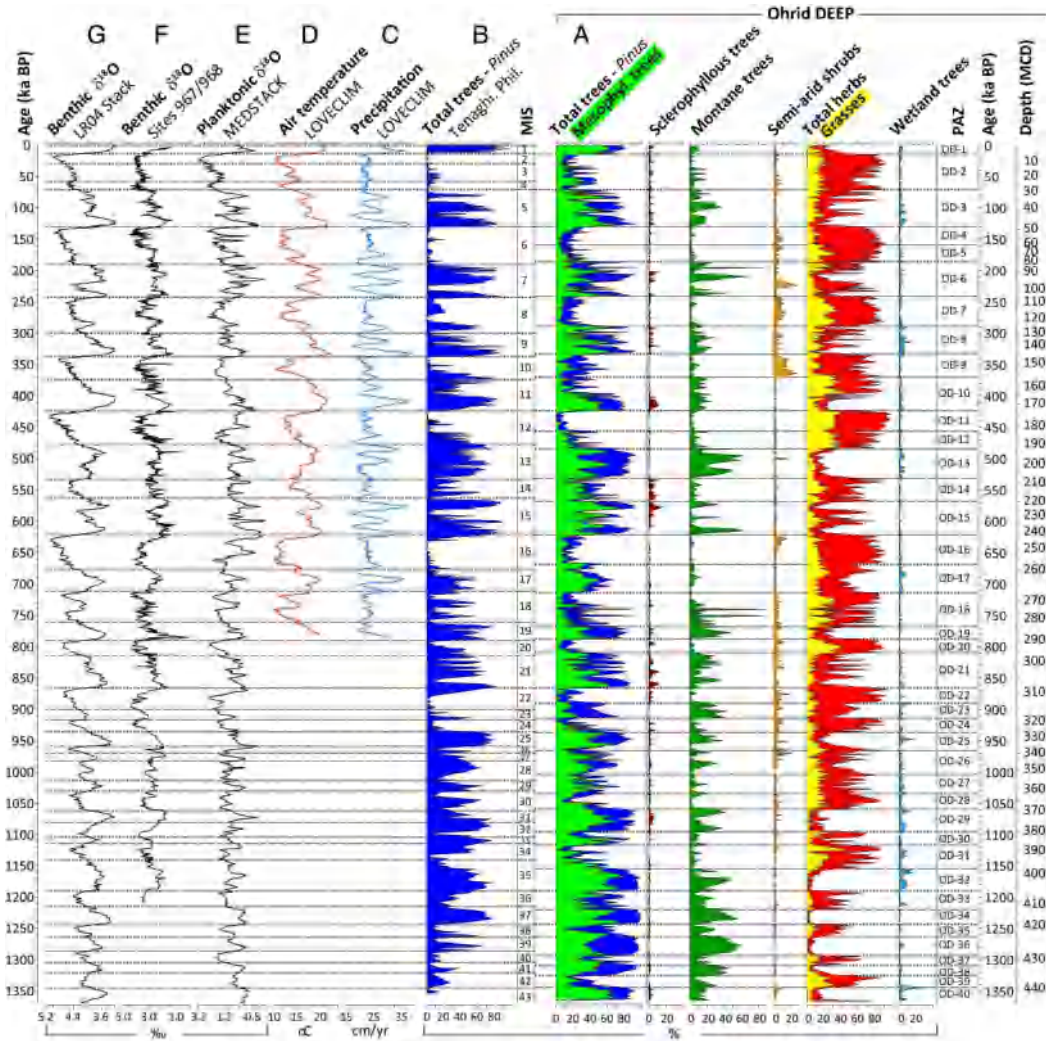


**Figure 2.** (A) Pollen diagram of ecological groups (%) against chronology of Wagner et al. (33): montane trees (*Abies*, *Betula*, *Cedrus*, *Fagus*, *Ilex*, *Picea*, *Taxus*, *Tsuga*); mesophyllous trees (*Acer*, *Buxus*, *Carpinus betulus*, *Carya*, *Castanea*, *Celtis*, *Corylus*, *Fraxinus excelsior/oxycarpa*, *Hedera*, *Ostrya/Carpinus orientalis*, *Pterocarya*, *Q. cerris*-type, *Q. robur*-type, *Tilia*, *Ulmus*, *Zelkova*); Sclerophyllous trees (*Arbutus*, *Cistus*, *Fraxinus ornus*, *Olea*, *Phillyrea*, *Pistacia*, *Quercus ilex*-type, *Rhamnus*); wetland trees (*Alnus*, *Liquidambar*, *Platanus*, *Populus*, *Salix*, *Tamarix*, *Taxodium*-type); and semiarid shrubs (*Ephedra*, *Ericaceae*, *Hippophaë*, *Cupressaceae* [mostly *Juniperus*-type]). (B) TP (location see Fig. 1): AP percentages excluding *Pinus*, *Betula*, and *Juniperus*-type (55–58, 60). (C) Model timeseries of annual precipitation and (D) mean SAT for the LO grid cell (33, 67). (E) MEDSTACK planktonic  $\delta^{18}\text{O}$  data (82). (F) Stacked benthic  $\delta^{18}\text{O}$  data for Ocean Drilling Program sites 967 and 968 from the eastern Mediterranean (83). (G) LR04  $\delta^{18}\text{O}$  global benthic stack (24).

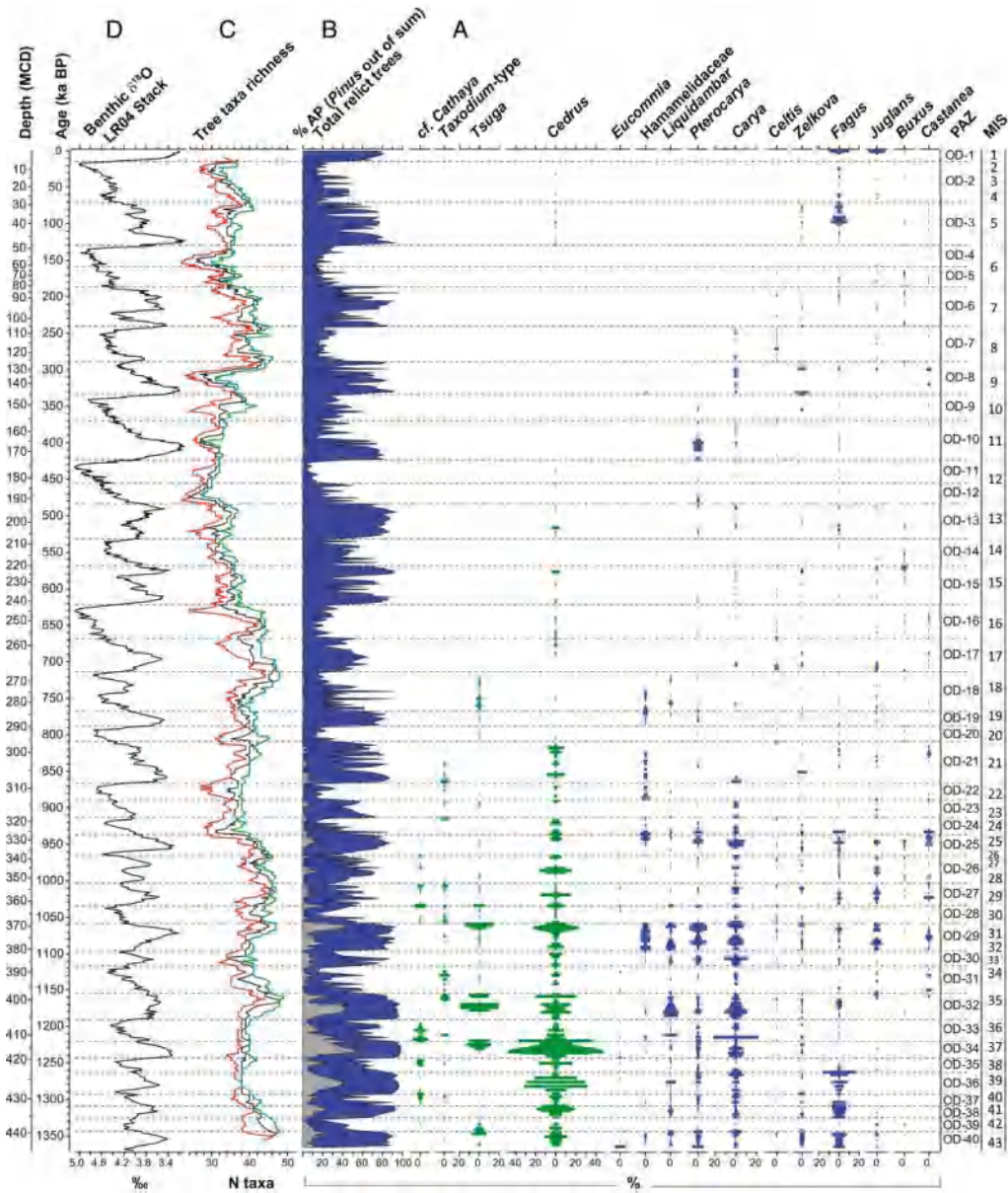


**Figure 3.** Relicts and richness. (A) Range and relative abundance of relict tree taxa in the DEEP site of LO together with (B) total % AP (filled blue) and % total relict taxa (filled gray, excl. Fagus). Bars represent % abundances for relict and rare tree taxa and are mirrored to enhance visibility. (C) Tree taxa richness of the DEEP site is based on taxa accumulation curves of tree pollen along a moving window. Single data points represent total richness from SAC (see Methods) with a sliding window of size 10 (red dotted line), 15 (black line), or 20 (green dashed line). All LO data are plotted against the chronology of Wagner et al. (33). (D) LR04  $\delta^{18}\text{O}$  global benthic stack (24).

## 5. SINOPROBE 剖面揭示的华南西北部安第斯型弧后前陆盆地系统



翻译人: 周洋 zhouy3@sustech.edu.cn

Li J H, Dong S W, Cawood P A, et al. *An Andean-type retro-arc foreland system beneath northwest South China revealed by SINOPROBE profiling [J]. Earth and Planetary Science Letters, 2018, 490: 170–179.*

<https://doi.org/10.1016/j.epsl.2018.03.008>

**摘要:** 在中生代, 华南地处欧亚板块和太平洋板块会聚边缘, 是了解弧后构造变形、沉积和岩浆相互作用的天然实验室。华南西北部的地壳结构在~600km 长的 SINOPROBE 深地震反射剖面显示, 从东向西为: (1) 扬子褶皱带上地壳褶皱变形强烈, 发育薄皮和厚皮构造, 记录了大规模的板内叠瓦式构造和挤压缩短; (2) 地壳尺度的近水平结构, 称为扬子拆离带, 为弱的粘性层, 以适应薄皮和厚皮构造系统中的应变和物质迁移; (3) 四川盆地几乎水平的反射层, 解释为弱变形沉积中心。扬子褶皱带和四川盆地代表了距大陆边缘岩浆弧>800 km 的弧后前陆盆地系统。我们认为整个岩浆弧和弧后系统的构造过程, 包括岩浆喷发、盆地沉积、弧后逆冲构造、岩石圈俯冲和与伸展相关的岩浆作用是相互关联的。年龄数据和地质关系将构造过程与古太平洋板块俯冲的地球动力学联系起来。

**ABSTRACT:** In the Mesozoic, South China was situated along the convergent margin between the Asian and Pacific plates, providing an excellent laboratory to understand the interactions between deformation, sedimentation and magmatism in a retro-arc environment. The crustal architecture of northwest South China is displayed along the ~600-km-long SINOPROBE deep seismic reflection profiles and reveals from east to west: (1) highly folded and truncated reflectors in the upper crust of the Yangtze Fold Zone, which correspond to thin- and thick-skinned thrust systems, and document large-scale intraplate structural imbrication and shortening; (2) a crustal-scale flat-ramp-flat structure, termed the Main Yangtze decollement, which forms a weak, viscous layer to accommodate strain decoupling and material transport in the thin- and thick-skinned systems; and (3) nearly flat-lying reflectors in the Sichuan Basin, which support interpretation of the basin as a weakly deformed depocentre. The Yangtze Fold Zone and the Sichuan Basin represent a retro-arc foreland basin

system that is >800 km away from the continental margin magmatic arc. We suggest that tectonic processes across the arc and retro-arc systems, including arc magma flare-up, basin sedimentation, retro-arc thrust propagation, lithosphere underthrusting, root foundering, and extension-related magmatism were interrelated and governed mass transfer. Age data and geological relations link the tectonic processes to evolving geodynamics of the subducting Paleo Pacific plate.

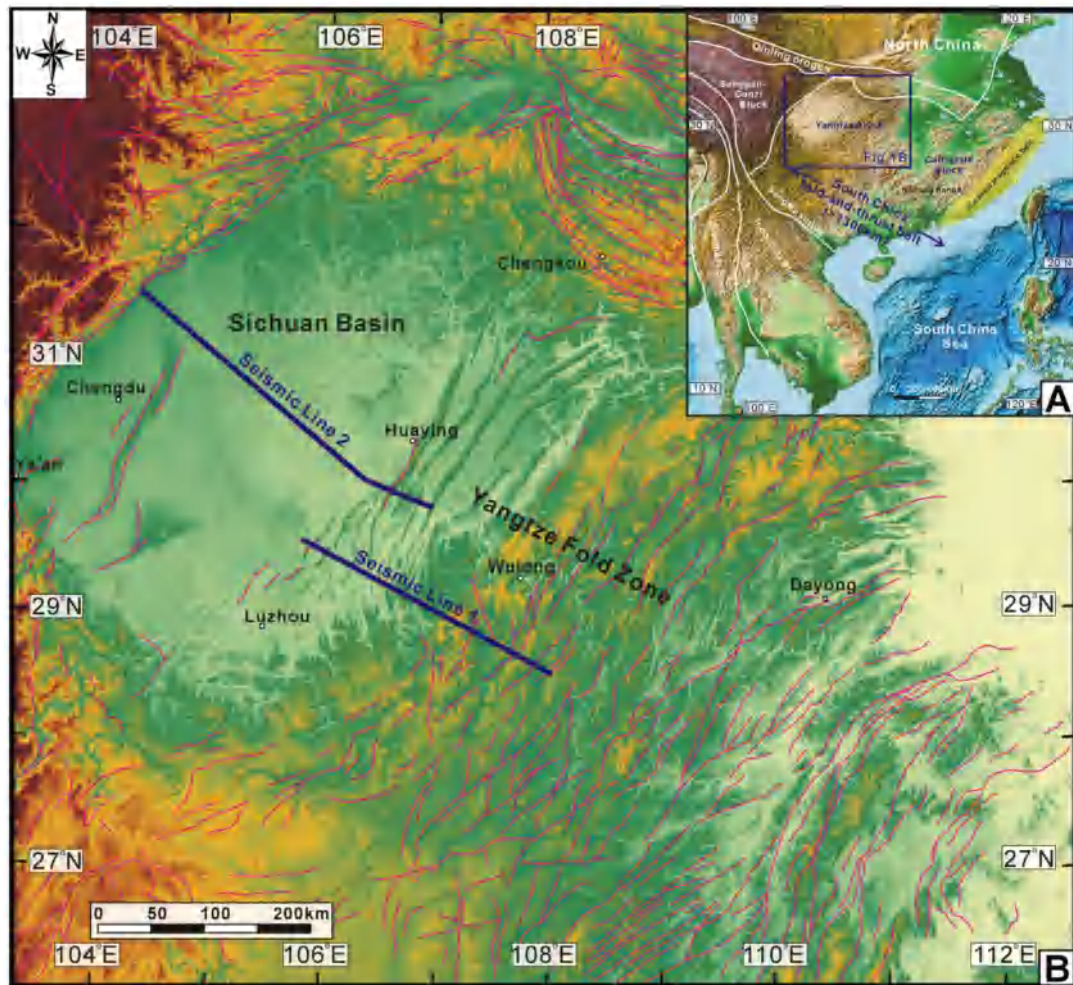


**Figure 1.** (A) Regional map of South China and surrounding area. Thick lines show boundary faults and suture zones, which were taken from Li et al. (2017). (B) Map of northwest South China showing regional structures and locations of seismic profiles.

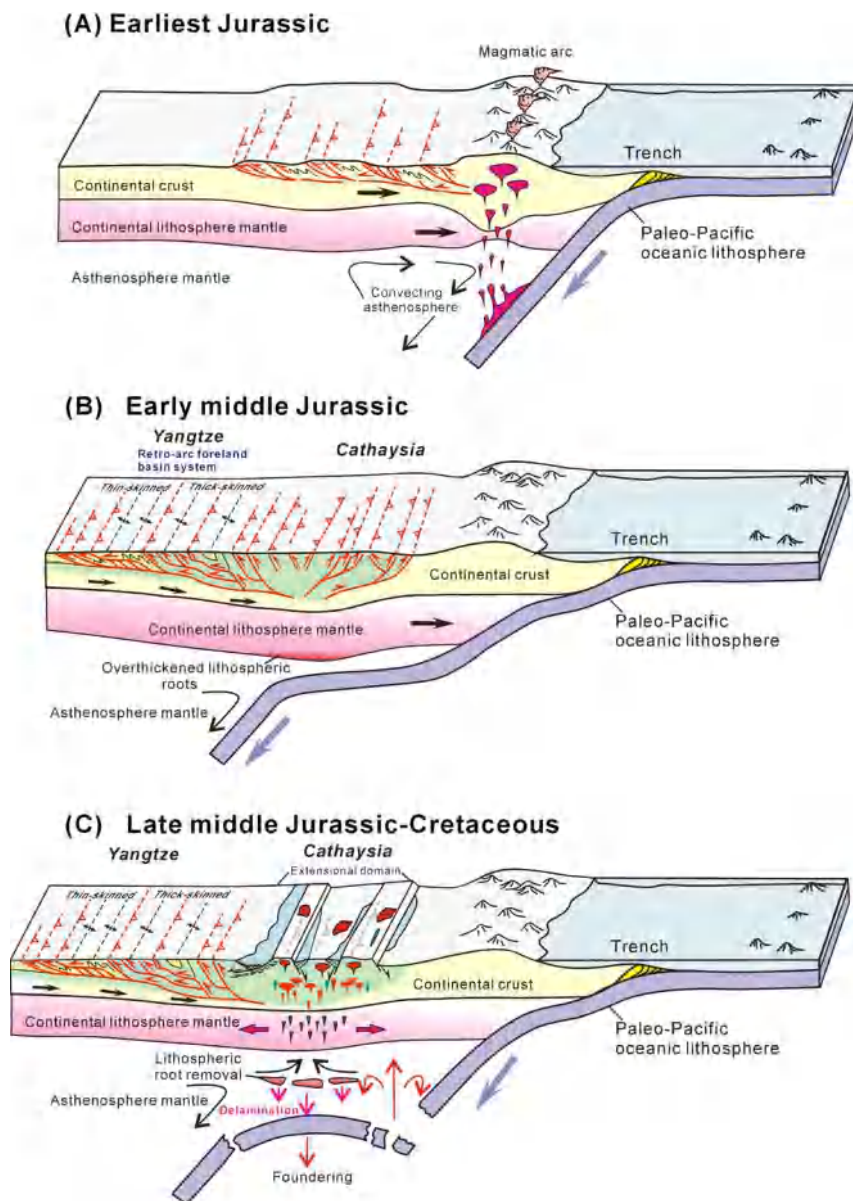


**Figure 2.** Sequential kinematic reconstruction for Jurassic development of the retro-arc foreland system in South China. (A) A magmatic arc flare-up and retro-arc thrusting occurred in the earliest Jurassic, associated with westward subduction of the Paleo-Pacific Plate. (B) A north-west-propagating, retro-arc foreland basin system formed in the Early middle Jurassic, in response to flat subduction of the Paleo-Pacific plate. Given that the crustal shortening mainly involved upper-crustal rocks, a slab of lower crust and lithosphere equal in length to upper-crustal shortening must have been underthrust eastward beneath the Cathaysia region. (C) The retro-arc foreland system underwent extension related tectono-thermal overprinting in Late middle Jurassic to Cretaceous time, possibly reflecting extensional collapse of the overthickened crust.

## 6. 海洋沉积物低温磁性特征-磁小体，超顺磁，磁赤铁矿化定量分析：以地中海东部为例



翻译人：张琪 zhangq7@sustech.edu.cn

Qian Y, Heslop D, Roberts A, et al, *Low-temperature magnetic properties of marine sediments – quantifying magnetofossils, superparamagnetism, and maghemitization: eastern Mediterranean examples* [J]. *Journal of Geophysical Research: Solid Earth*, 2021, e2021JB021793.

<https://doi.org/10.1029/2021JB021793>

**摘要：**地中海东部海洋沉积物周期性且显著的氧化还原环境的变化驱动环境和成岩作用发生改变，磁性矿物对这种改变十分敏感。因此，磁性特征的变化为富含有机质的沉积物(腐泥)在沉积时以及沉积之后的古海洋环境提供了有用的指示。针对地中海东部沉积物在室温下的磁学性质研究已经开展了几十年；然而，很少有研究考虑到低温磁性特征。本文，作者研究了来自地中海东部不同类型沉积物的低温（10 至 300 K）磁性特征，结合室温（~ 300 K）磁学特征，透射电子显微镜，以及校准 X-射线荧光元素数据，用以说明可以从对沉积物的低温磁学性质分析中获得有价值的信息。低温磁学研究结果表明，磁小体化石和超顺磁磁铁矿颗粒在地中海东部沉积物中广泛存在。超顺磁颗粒在含有腐泥的成岩还原层段中含量最高。与此相反，磁小体化石在腐泥的顶部氧化带前锋线最为丰富，形成了强烈的氧化还原梯度，但它同时也广泛分布于其他未受严重还原成岩作用的沉积区间。此外，在腐泥顶部的氧化锋面和其他含氧沉积层段，磁铁矿颗粒表面被磁化（即部分氧化）。研究结果表明，研究古海洋学和古环境过程时，低温磁性测量在定量研究不同的沉积磁信号方面具有一定的价值。

**ABSTRACT:** Periodic and marked redox changes in eastern Mediterranean marine sediments drive environmental and diagenetic changes to which magnetic minerals are sensitive. Magnetic property changes, therefore, provide useful indications of paleoceanographic conditions during and after periods of organic-rich sediment (sapropel) deposition. Magnetic properties of eastern Mediterranean sediments at room temperature have been studied for decades; however, few studies have considered low-temperature magnetic properties. Here, we investigate the low-temperature (10 to 300 K) magnetic properties of different eastern Mediterranean sediment types combined with room temperature (~300 K)

magnetic properties, transmission electron microscopy, and calibrated X-ray fluorescence elemental data to illustrate the valuable information that can be obtained from low-temperature magnetic analysis of sediments. Our low-temperature magnetic results suggest that magnetite magnetofossils and superparamagnetic particles occur widely in eastern Mediterranean sediments. Superparamagnetic particle contents are highest in diagenetically reduced intervals associated with sapropels. In contrast, magnetite magnetofossils are most abundant in oxidation fronts at the tops of sapropels, where strong redox gradients formed, but are also widespread throughout other sedimentary intervals that have not been subjected to extensive reductive diagenesis. Moreover, the surfaces of magnetite particles are maghemitized (i.e. partially oxidized) in oxidation fronts at the tops of sapropels, and in other oxic sediment intervals. Our results demonstrate the value of LT magnetic measurements for quantifying diverse sedimentary magnetic signals of interest in environmental magnetism when studying paleoceanographic and paleoenvironmental processes.

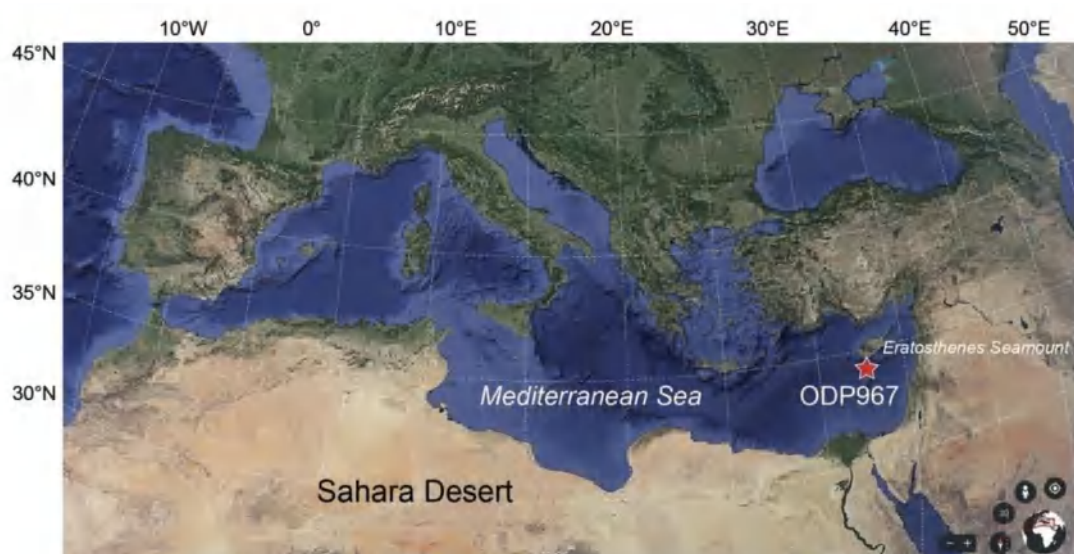


**Figure 1.** Location of ODP Site 967 (34°04'N, 32°43'E, 2,553 m water depth) and Eratosthenes Seamount (map generated from Google Earth).

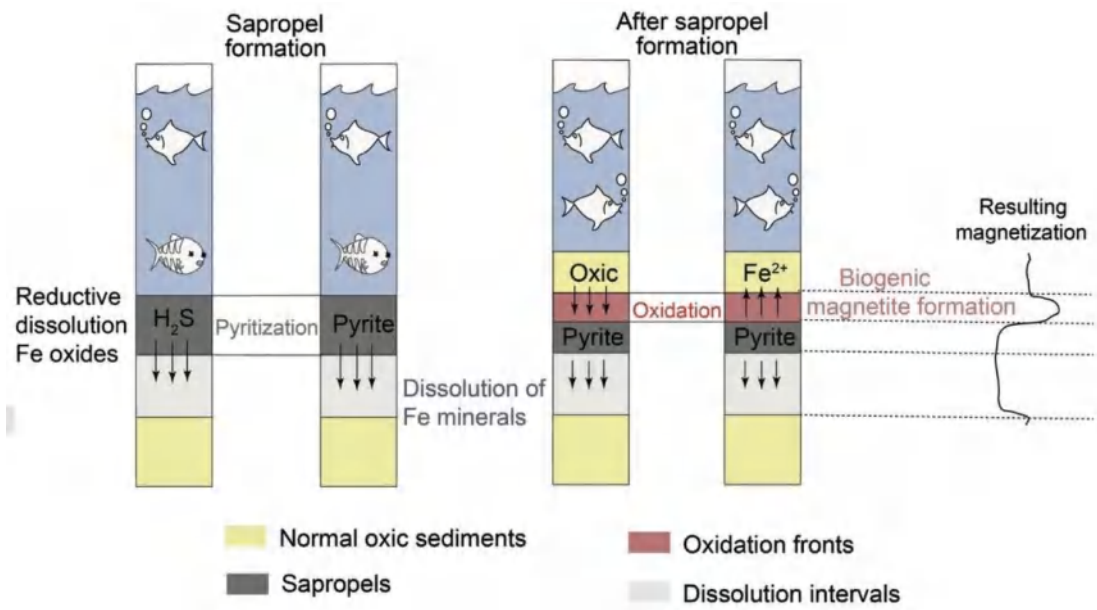


**Figure 2.** Illustration of sapropel formation and magnetization (e.g., ARM) variations in the eastern Mediterranean Sea (characteristic of a Type 2 sapropel).

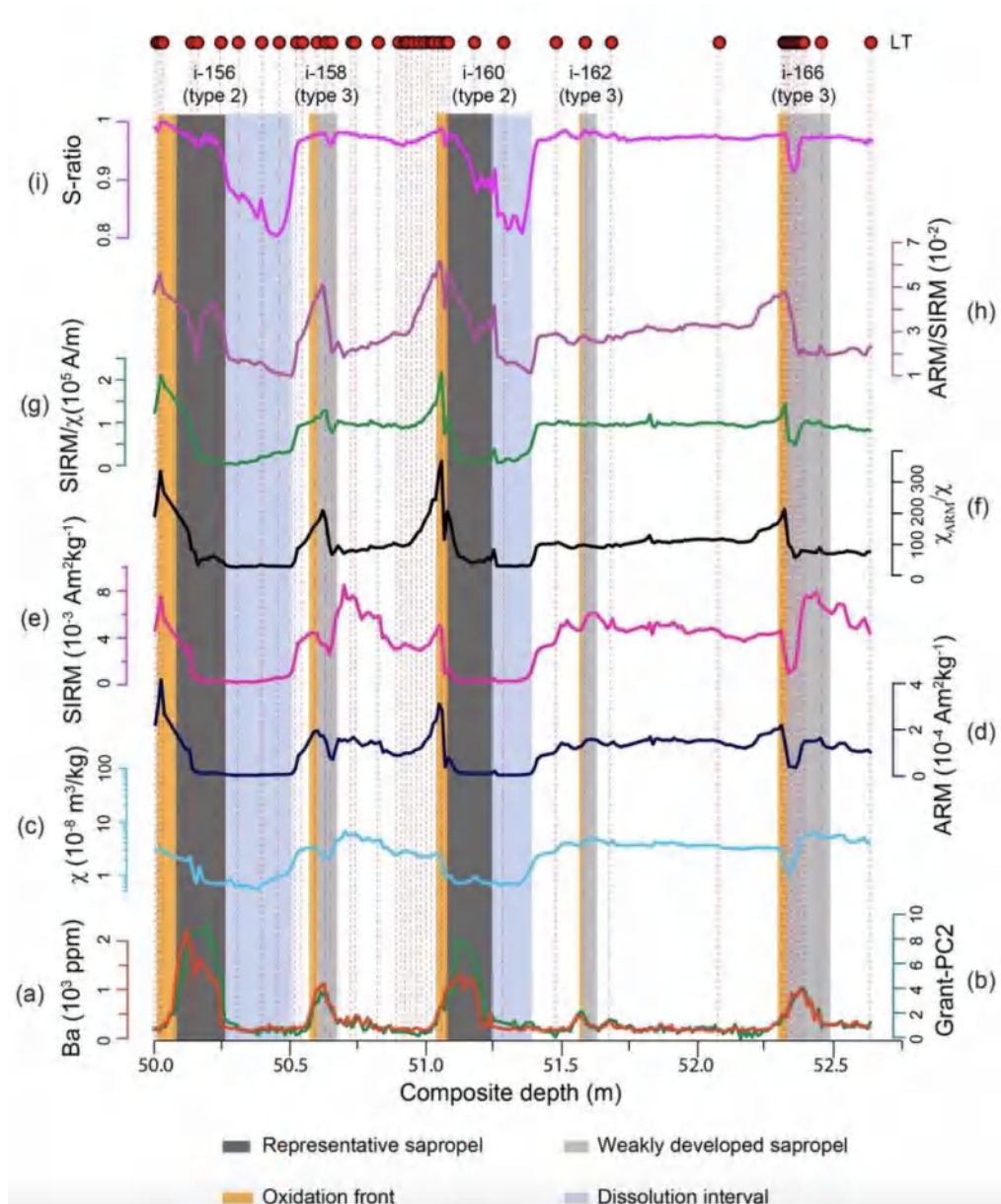


**Figure 3.** Down-core variations of geochemical data and environmental magnetic parameters. Elevated (a) Ba (orange) and (b) Grant-PC2 (dark green) indicate the positions of sapropels. Discrete sample data include (c)  $\chi$  (cyan); (d) ARM (dark blue); (e) SIRM (pink); (f)  $\chi_{\text{ARM}}/\chi$  (black); (g) SIRM/ $\chi$  (green); (h) ARM/SIRM (purple); and (i) S-ratio (magenta). Forty-four samples selected for LT analyses are indicated by red circles at the top of the figure. Dark gray and light gray shadings denote the locations of representative and weakly developed sapropels, respectively. Orange and blue shadings correspond to the locations of oxidation fronts and dissolution intervals, respectively. Sapropel stratigraphy is based on Emeis et al. (2000), where the numeric number followed by “i-” is the insolation cycle. Modified from Qian et al. (2020).

## 7. 伴随沉积放大效应的南大洋过程造成冰期碳循环变化



翻译人：盖聪聪 gaicc@sustech.edu.cn

Kobayashi H, Oka A, Yamamoto A, et al. *Glacial carbon cycle changes by Southern Ocean processes with sedimentary amplification* [J]. *Science Advances*, 2021(7), eabg7723.

<https://doi.org/10.1126/sciadv.abg7723>

**摘要:** 最近的古重建表明,冰期南大洋碳储存量的增加导致了冰期大气二氧化碳浓度 ( $p\text{CO}_2$ ) 的降低。然而,用三维大洋环流模型 (OGCM) 来量化其贡献具有挑战性。作者通过 OGCM 对沉积过程进行模拟,模拟过程考虑了冰期南大洋盐度分层的增强和冰川粉尘造成的铁肥化,提高了冰期深层水 (具有碳同位素偏轻、低氧和老碳年龄的特征) 的模型数据一致性。冰期模拟显示大气  $p\text{CO}_2$  降低 77 ppm,这与古记录非常吻合。南大洋盐度分层和冰川粉尘的铁肥作用放大了碳酸盐的沉积反馈,这一反馈会导致深海碳储量的大部分增加,并对  $p\text{CO}_2$  的降低具有重要作用。南大洋性质的模型和数据一致性对于模拟海洋碳循环在冰期时的变化至关重要。

**ABSTRACT:** Recent paleo reconstructions suggest that increased carbon storage in the Southern Ocean during glacial periods contributed to low glacial atmospheric carbon dioxide concentration ( $p\text{CO}_2$ ). However, quantifying its contribution in three-dimensional ocean general circulation models (OGCMs) has proven challenging. Here, we show that OGCM simulation with sedimentary process considering enhanced Southern Ocean salinity stratification and iron fertilization from glaciogenic dust during glacial periods improves model-data agreement of glacial deep water with isotopically light carbon, low oxygen, and old radiocarbon ages. The glacial simulation shows a 77-ppm reduction of atmospheric  $p\text{CO}_2$ , which closely matches the paleo record. The Southern Ocean salinity stratification and the iron fertilization from glaciogenic dust amplified the carbonate sedimentary feedback, which caused most of the increased carbon storage in the deep ocean and played an important role in  $p\text{CO}_2$  reduction. The model-data agreement of Southern Ocean properties is crucial for simulating glacial changes in the ocean carbon cycle.

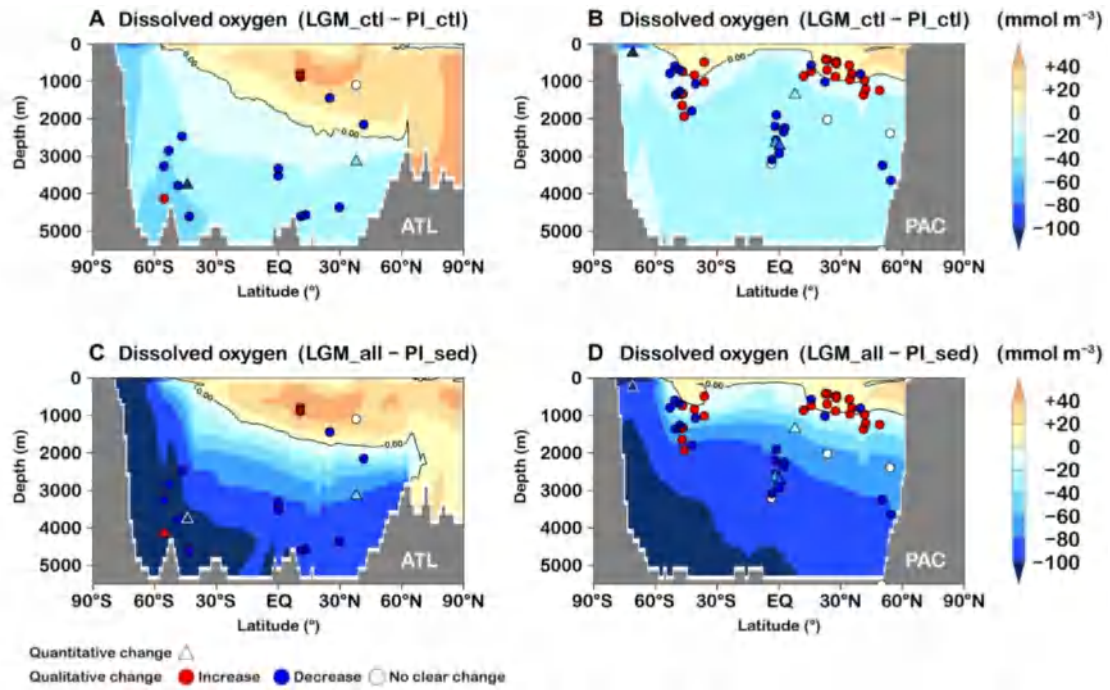


**Figure 1.** Glacial changes in dissolved oxygen. Model-data comparisons of zonal mean changes in dissolved oxygen ( $\text{mmol m}^{-3}$ ) from PI\_ctl to LGM\_ctl in the (A) Atlantic and (B) Pacific. (C and D) Same as (A) and (B) except for changes from PI\_sed to LGM\_all.

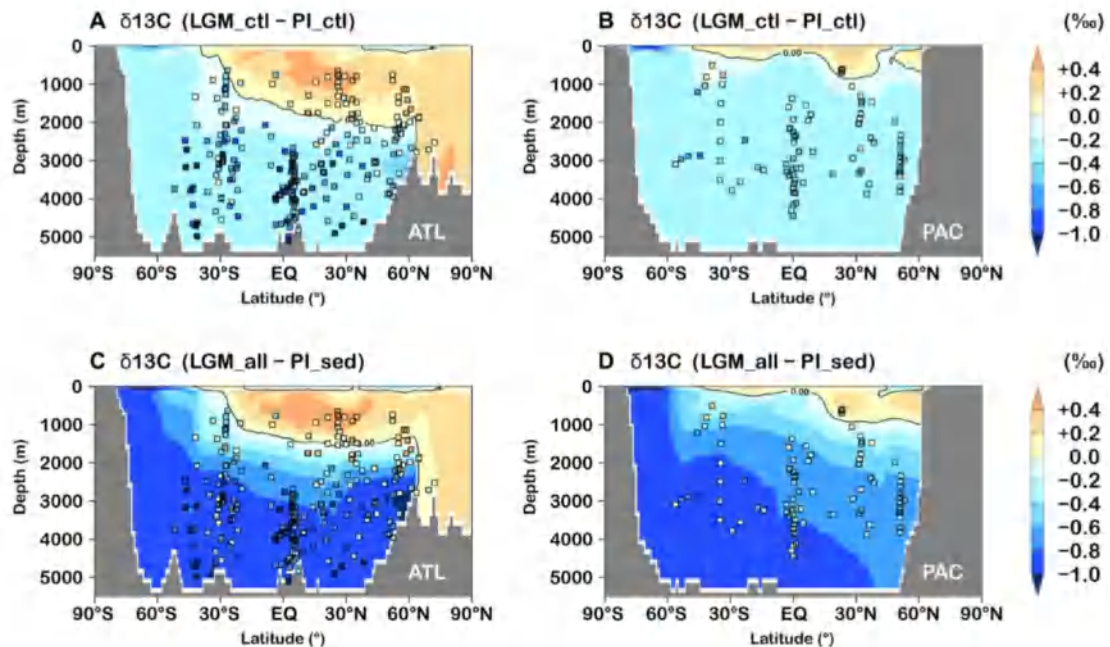


**Figure 2.** Glacial changes in  $\delta^{13}\text{C}$ . Model-data comparisons of zonal mean changes in  $\delta^{13}\text{C}$  (‰) from PI\_ctl to LGM\_ctl in the (A) Atlantic and (B) Pacific with paleo records (squares). (C and D) Same as (A) and (B) except for changes from PI\_sed to LGM\_all.

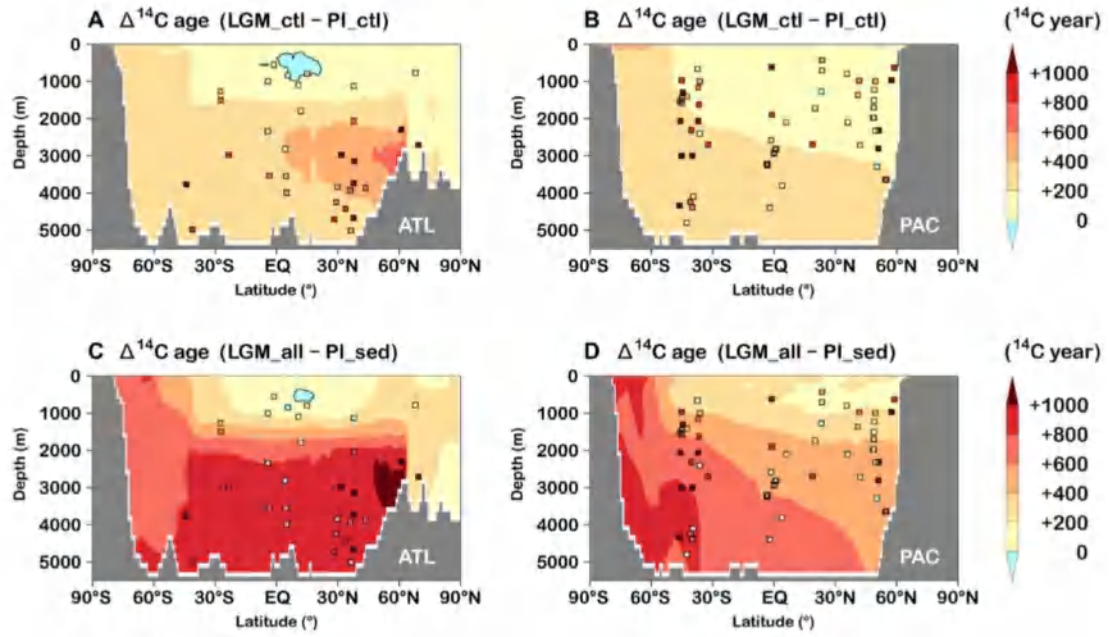


**Figure 3.** Glacial changes in radiocarbon ages. Model-data comparisons of zonal mean changes in radiocarbon ages ( $^{14}\text{C}$  year) from PI\_ctl to LGM\_ctl in the (A) Atlantic and (B) Pacific with paleo records (squares). (C and D) Same as (A) and (B) except for changes from PI\_sed to LGM\_all.

## 8. 巴拉望中南部古近系裂陷期沉积物的地层特征和物源:对华南陆缘的古地理重建意义



翻译人: 刘伟 inewway@163.com

Chen WH, Yan Y, Carter A, et al. *Stratigraphy and provenance of the Paleogene syn-rift sediments in central-southern Palawan: Paleogeographic significance for the South China margin* [J].

*Tectonics*, 2021, online.

<https://doi.org/10.1029/2021TC006753>

**摘要:** 南海海底的扩张造成巴拉望微陆块与华南陆缘的分离。然而, 巴拉望微陆块从华南陆缘分离的时间和具体位置尚不明确, 分离之前的沉积路径尚不清楚。为此, 我们对巴拉望中南部 Panas-Pandian 组裂陷期沉积岩进行了生物地层和物源的研究。微体古生物学证据表明, Panas-Pandian 组为中始新世-早渐新世 (47.7 ~ 32.9 Ma)。基于此, 结合后裂陷期 Nido 灰岩最古老的年龄 (32 Ma), 巴拉望微陆块的破裂不整合面年龄被确定为 33-32 Ma。该破裂不整合时间与珠江口盆地 (30 Ma) 和 IODP U1435 (34Ma) 的不整合时间接近, 表明巴拉望微陆块与珠江口盆地具有共轭关系。Panas-Pandian 组的遗迹化石和底栖有孔虫显示了华南陆缘陆坡的半深海至深海环境。多学科物源分析表明, Panas-Pandian 组既来自局部中生代基底隆起, 也来自华夏地块内部的物源。结果表明, 至少在中始新世 (47.7 ~ 42.1 Ma) 以来, 已形成了一条古珠江, 可以将华夏地块内部的沉积物跨越低地形梯度的裂陷边缘搬运到陆坡。

**ABSTRACT:** The Palawan microcontinental block is thought to have separated from the South China margin due to seafloor spreading and opening of the South China Sea. However, it is uncertain when and from which section the Palawan microcontinental block rifted from the South China margin, and little is known about sediment routing across the rifted margin before continental breakup. To address these aspects we studied the biostratigraphy and provenance of syn-rift sedimentary rocks collected from the Panas-Pandian Formation in central-southern Palawan. Micropaleontological evidence indicates a Middle Eocene–earliest Oligocene (47.7–32.9 Ma) age for the Panas-Pandian Formation. Based on this and the oldest age of the post-rift Nido Limestone

(~32 Ma), the breakup unconformity on the Palawan microcontinent block is dated around 33–32 Ma. This timing of breakup unconformity is close to that of the Pearl River Mouth Basin (~30 Ma) and IODP Site U1435 (~34Ma), suggesting the conjugate relationship between the Palawan microcontinental block and the Pearl River Mouth Basin. Trace fossils and benthic foraminifera from the Panas-Pandian Formation indicate a middle bathyal to abyssal environment on the continental slope of the South China margin. Multidisciplinary provenance analysis reveals that the Panas-Pandian Formation was derived from both local Mesozoic basement uplifts and the interior Cathaysia Block. It indicates that a paleo-Pearl River has been established at least since the Middle Eocene (47.7–42.1 Ma) and could deliver sediments from the interior Cathaysia Block to the continental slope, across the wide rifted margin with a low topographic gradient.

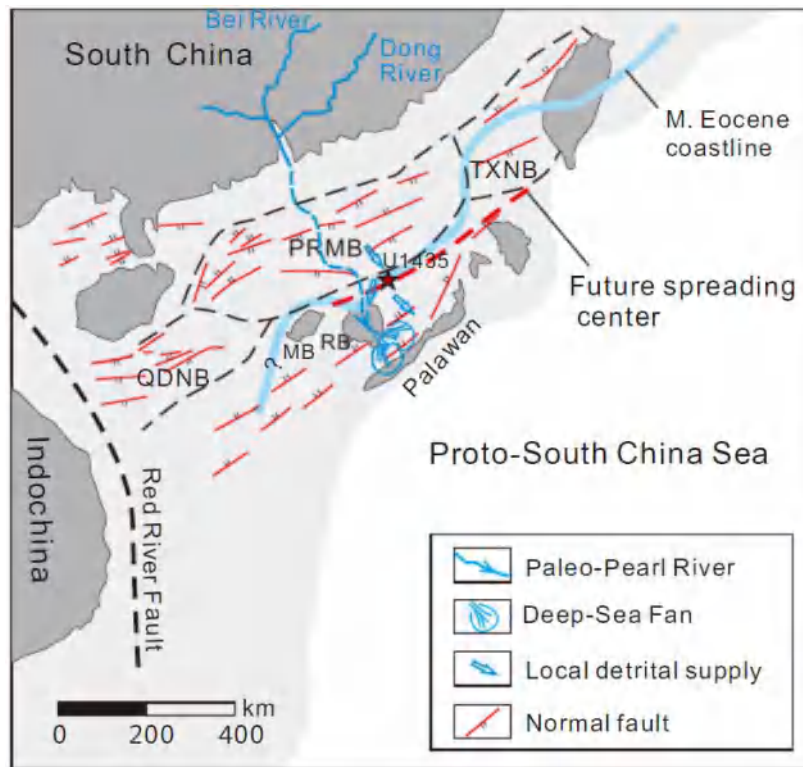


**Figure 1.** Paleogeographic reconstruction for the South China margin during the Middle Eocene (47.7–42.1 Ma) (revised from Hall, 2002, 2012; Li et al., 2017), showing two source regions for the Panas-Pandian Formation, a proximal source from the Mesozoic basement uplift and a distant source from the interior Cathaysia Block. The inferred Middle Eocene coastline is mainly based on Huang et al. (2019), Li et al (2017) and Yao et al. (2012). PRMB=Pearl River Mouth Basin; QDNB=Qiongdongnan Basin; TXNB=Taixinan Basin; RB=Reed Bank; MB=Macclesfield Bank.

## 9. 来自中国中部重庆的 40000 年的植被、环境和气候 变化记录



翻译人: 杨会会 11849590@mail.sustech.edu.cn

Dodson J, Shi G, Lu F Y, et al., *A 40,000 year record of vegetation, environment and climate change from Chongqing, Central China [J]. Palaeogeography, Palaeoclimatology, Palaeoecology*, 2021,573,110441.

<https://doi.org/10.1016/j.palaeo.2021.110441>

**摘要:** 丛平湿地位于重庆市境内, 海拔 2100 米左右。它被一片灌木丛生的草地所包围, 逐渐变成针叶树和落叶林的混合林地。基于花粉、微炭和地球化学的记录已经被用来重建过去大约 40 kyr BP 的环境历史。在整个记录中, 该地点都是树木繁茂的, 有两个相对温暖的时期: MIS3 和全新世约 9 kyr BP 以来。在 27 - 18 kyr BP 出现逐渐降温的过程, 其中最冷的时期是 22 - 18 kyr BP 出现的针叶林冷暖混交林。常绿落叶混交林出现时气温最高, 为 9 ~ 1.5 kyr BP。总体变化规律与湖北大九湖花粉记录一致, 表明这是一个区域信号。末次冰盛期 (LGM) 中国中部地区的湿润表明, 东亚夏季风给大陆带来了足够的水分维持森林覆盖, 即使在 2120 米的海拔。大尺度的变化被解释为与地球轨道参数的变化和南海海平面的变化有关, 这些变化对中国中部的水汽输送有影响。据推测, 造成中国东北干燥气候的西风带截留了足够的夏季风, 使中国中部保持湿润。新仙女木事件 (YD) 出现在风化指标中, 从沉积物元素丰度的几个变化中可以明显看出来。丛平湿地的记录显示, 没有明确的证据表明人类活动对其植被造成了影响, 当地也没有发生过任何引起植被变化的山火。在过去 1.5 kyr BP 轻微的降温导致针叶树数量增加, 阔叶树数量减少, 风化速率增加。

**ABSTRACT:** Congping is a wetland at about 2100 m asl in Chongqing Province. It is surrounded by a shrubby grassland which grades into a mixed conifer and deciduous woodland. A record based on pollen, microcharcoal and geochemistry has been used to reconstruct an environmental history covering the last approximately 40 kyr BP. The site was wooded throughout the entire record and there were two relatively warm periods; during Marine Isotope 3 (MIS 3) and for the Holocene from about 9 kyr BP. From 27 to 18 kyr BP a gradual cooling occurred and the coldest part of the record was between 22 and 18 kyr BP when a mixed conifer cool temperate deciduous forest occurred, The

warmest part of the record lasted from about 9 to 1.5 kyr BP when mixed evergreen and deciduous forest occurred. The broad pattern of changes is in accord with pollen records from Dajiuhu in Hubei, and demonstrates that this was a regional signal. A moist central China at Last Glacial Maximum (LGM) shows that the East Asian Summer Monsoon was delivering enough moisture on the mainland to sustain forest cover, even at 2120 m asl. The large-scale changes are interpreted as relating to changes in Earth's orbital parameters and sea-level changes in the South China Sea which had an impact on moisture delivery into central China. It is surmised that the westerlies which created dry climates in northeastern China trapped the summer Monsoon influence enough to keep central China moist. The Younger Dryas (YD) is present in the weathering parameters as evident in several changes in elemental abundance delivered to the sediments. The Congping record shows no clear evidence of human impact on its vegetation, and there were no local fires to have caused any vegetation changes. In the last 1.5 kyr BP a slight cooling caused a rise in conifers, a decline in broad-leaved tree taxa and increased weathering rates.

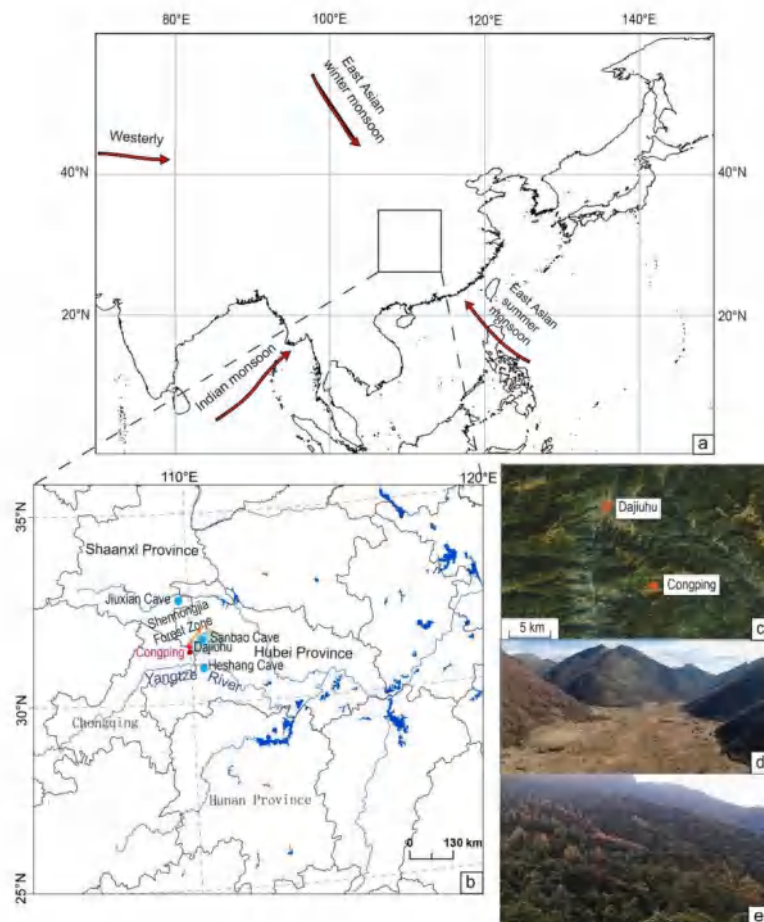


**Figure 1.** a. Map of central China showing mean positions of major monsoon systems at the present time. b. Map of central China showing key sites mentioned in the text. c. Image showing the relative locations of Congping (Chongqing) and Dajiuhu (Hubei). d. View across Congping wetland showing the steep slopes which surround the site. e. Mixed deciduous and conifer forest which surrounds the site.

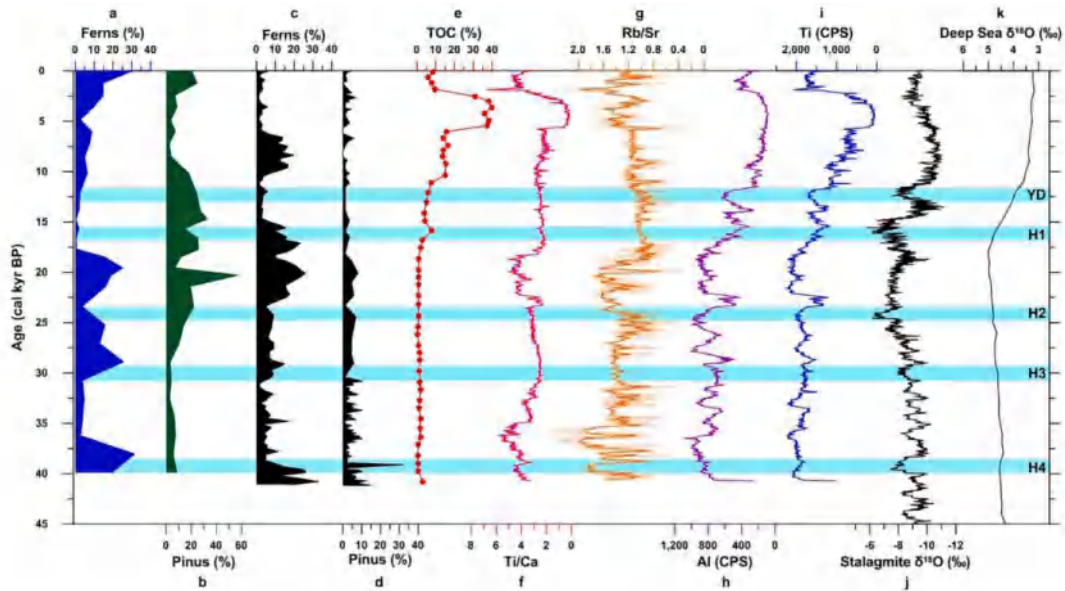


**Figure 2.** Plot of selected parameters of environmental change in the China region, including some parameters from the Congping records. Curves a and b, from the present study, curves c and d from Dajiuhu (Li et al., 2013), curves e to I from the present study, i: stalagmite record from Cheng et al. (2016) and j: Deep Sea record from Lisiecki (2005).

## 10. 马达加斯加西北部石笋记录揭示了 8.2 ka 事件的时间和特征



翻译人: 李海 12031330@mail.sustech.edu.cn

Duan P, Li H, Sinha A, et al. *The timing and structure of the 8.2 ka event revealed through high-resolution speleothem records from northwestern Madagascar [J]. Quaternary Science Reviews, 2021, 268, 107104.*

<https://doi.org/10.1016/j.quascirev.2021.107104>

**摘要:**尽管 8.2 ka 事件是一个众所周知的全球均有记录的气候突变事件, 但其在非洲东南部热带地区的详细记录较少。作者展示了马达加斯加西北部石笋 (ABC-1) 的 8.5-7.5 ka 高分辨率的水文气候变化记录。结合方解石出现的层位 (指示更潮湿的条件), ABC-1 的  $\delta^{18}\text{O}$  记录 8.230-8.053 ka 明显负偏指示一个湿的 8.2 ka 事件。该事件的特点是将  $\delta^{18}\text{O}$ - $\delta^{13}\text{C}$  的短期 (年际到年代际) 相关性转换为长期 (数十年至百年) 相关性, 表明 8.2 ka 事件期间森林系统稳定且发育良好。研究结果揭示了 8.2 ka 事件的两阶段特征, 每个阶段都叠加了两个短暂的降雨事件。在第一阶段广泛记录的两个峰/谷表明气候信号最初通过淡水强迫触发的大气过程迅速传播, 而第二阶段的峰/谷在不同气候系统中的不同行为可能表明不同的强迫。

**ABSTRACT:** Although the 8.2 ka event is a well-known globally documented abrupt climate event, its detailed expression in tropical southeastern Africa is poorly constrained. Here we present a high resolution and precisely dated record of the regional hydroclimatic variability between 8.5-7.5 ka BP from a polymorphic speleothem (ABC-1) from northwestern Madagascar. In combination with the exclusive recurrences of calcite layers (indicative of wetter conditions), the distinctly negative excursions in the ABC-1  $\delta^{18}\text{O}$  record manifest a wet 8.2 ka event that spanned from 8.230 to 8.053 ka BP. The event is characterized by the replacement of shorter-term (interannual to interdecadal)  $\delta^{18}\text{O}$ - $\delta^{13}\text{C}$  coherence with the longer-term (multidecadal to centennial) coherence, suggesting a stable and well-developed forest system during the 8.2 ka event. Our data reveal a two-stage structure of the 8.2 ka event, which is superimposed with two brief pluvial episodes in each stage. The widely documented two peaks/troughs during Stage-I suggest rapid propagation of climate

signal through atmospheric processes triggered initially by the freshwater forcing, whereas the divergent behaviors of the peaks/troughs in Stage-II in different climate systems may suggest a different forcing.

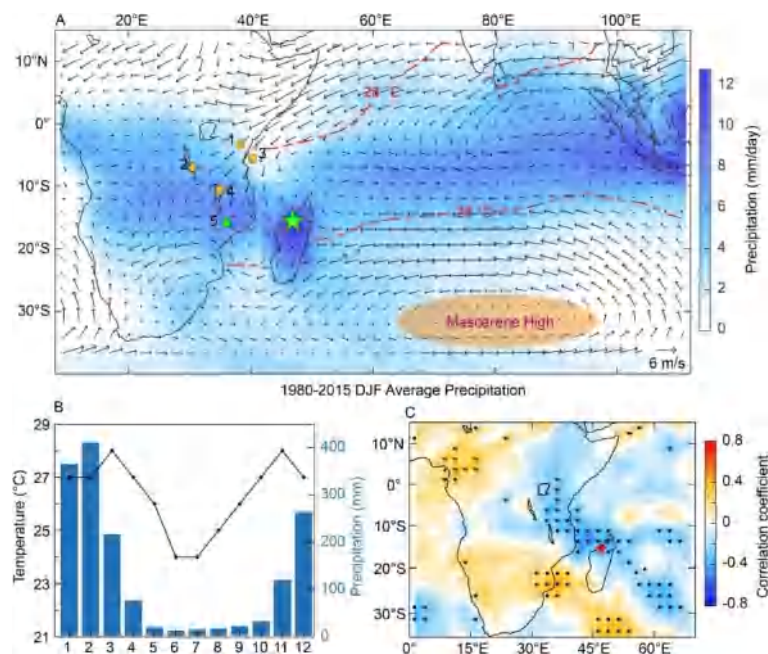


**Figure 1.** Climatology and proxy locations. (A) Spatial pattern of near-surface (850 hPa) winds (arrows) and average precipitation rates (blue shading) for December-January-February (DJF) estimated by Global Precipitation Climatology Project monthly analysis (GPCP v2.3) dataset from 1980 to 2015. The 28°C isotherm of SST is indicated by the red dashed line and the Mascarene High is highlighted by shading ellipse. Locations of Anjohibe Cave (green star) and mentioned records in the text (solid circles) are marked as: (1) Kilimanjaro plateau, (2) Lake Tanganyika, (3) GeoB12605-3, (4) Lake Malawi, (5) Lake Chilwa. Yellow and green circles indicate dry and wet conditions during the 8.2 ka event. (B) Climograph of NW Madagascar (15-16°S, 46-47°E) for 1901-2018 from Climate Research Unit Time Series version 4.03 (CRU TS4.03) gridded reanalysis dataset which has a horizontal resolution of 0.5° × 0.5° (Harris et al., 2014). Blue bars and black squares connected with black lines indicate monthly precipitation and temperature, respectively. (C) Spatial correlation between amount weighted  $\delta^{18}\text{O}_p$  DJF nearest to the cave site derived from IsoGSM (Yoshimura et al., 2008) and precipitation elsewhere from GPCP between 1980 and 2015. Stippling indicates sites with significant correlation ( $p < 0.1$ ). The location of Anjohibe Cave is marked by a red star. (For interpretation of the references to color in this figure legend, the reader is referred to the Web version of this article.)

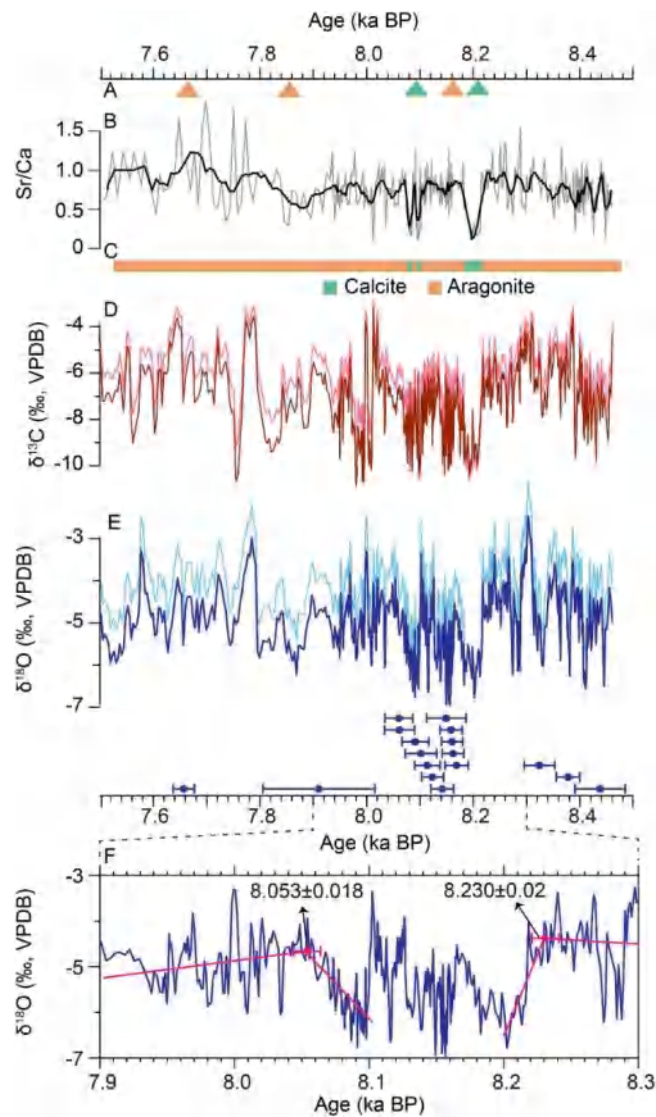


**Figure 2.** Results and breakpoint analysis for speleothem ABC-1. All profiles are in MOD-AGE age model. (A) Mineralogy was identified by X-ray diffraction at depths of 86, 93, 161, 134 and 170 mm. Orange and green triangles indicate aragonite and calcite layers, respectively. (B) Sr/Ca ratio record (gray) with 8-point running average (black). (C) Inferred mineralogy based on X-ray diffraction estimations and trace element results. Green and orange mark the portions of calcite and aragonite layers, respectively. (D) Raw (pink) and corrected (brown) carbon isotope records. (E) Raw (light blue) and corrected (dark blue) oxygen isotope records together with the  $^{230}\text{Th}$  dating results ( $2\sigma$ ) marked by blue circles and error bars. (F) The breakpoints estimation (Mudelsee, 2009) of the 8.2 ka event for ABC-1  $\delta^{18}\text{O}$  profiles between 8.3 and 7.9 ka BP. The change points and associated  $2\sigma$  errors (relative to the MOD-AGE age model chronology) are marked by red solid circles with vertical bars and ages. (For interpretation of the references to color in this figure legend, the reader is referred to the Web version of this article.)

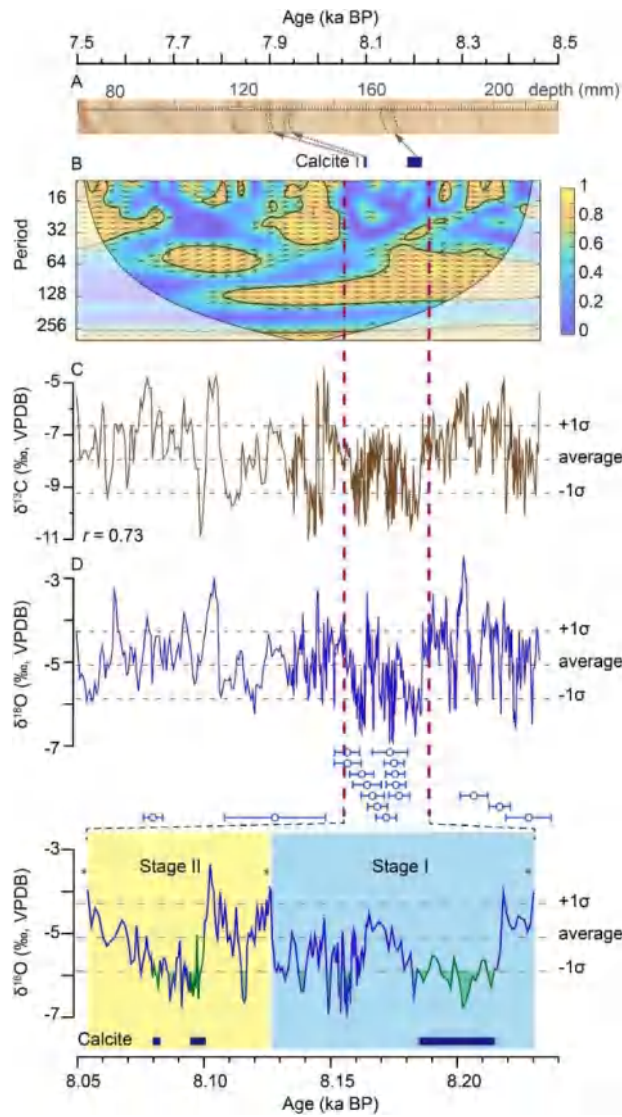


**Figure 3.** Speleothem ABC-1  $\delta^{18}\text{O}$  and  $\delta^{13}\text{C}$  profiles and coherence analysis. (A) The image of speleothem ABC-1 between 70 and 220 mm. Dark blue bars in the time domain correspond to the calcite layers highlighted by dashed lines in the image. (B) Squared wavelet coherence between  $\delta^{18}\text{O}$  and  $\delta^{13}\text{C}$ . The 5% significance level against red noise and phase relationship is shown as a thick contour and arrows. (C and D) The ABC-1  $\delta^{13}\text{C}$  and  $\delta^{18}\text{O}$  records with the average and  $1\sigma$  values marked by dashed lines. 230Th dates with  $2\sigma$  error are indicated by blue circles and bars. The purple dashed lines from B-D indicate the 8.2 ka event. The inset is same as D but between 8.24 and 8.05 ka BP (calcite layers indicated by dark blue bars below are marked in green in  $\delta^{18}\text{O}$  record). Stage-I and Stage-II are shaded by blue and yellow bars. Green shading highlights the episodes with  $\delta^{18}\text{O}$  values lower than  $-1\sigma$  from the mean. (For interpretation of the references to color in this figure legend, the reader is referred to the Web version of this article.)

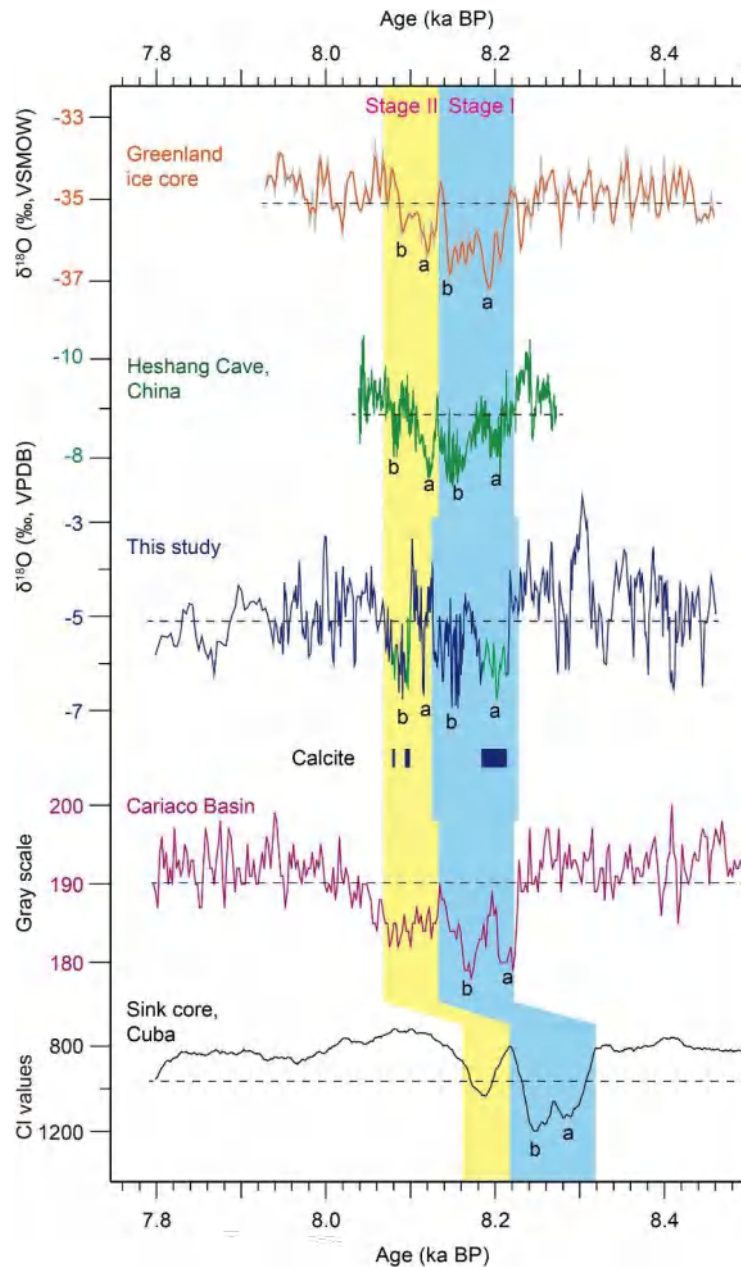


**Figure 4.** Paleoclimate comparison during the 8.2 ka event. From top to bottom are  $\delta^{18}\text{O}$  records from Greenland ice core (gray) and 10-year moving average (orange) (Thomas et al., 2007), speleothem HS4 from Heshang Cave (green) (Liu et al., 2013), speleothem ABC-1 from Anjohibe Cave (this study), the gray-scale record (purple) from the Cariaco Basin (Hughen et al., 1996) and Cl value record from the Cuban sinkhole (black) (Peros et al., 2017). Blue and yellow bars are as in Fig. 4 (in the text). The dashed lines in each subpanel indicate the average values for the presented period. The letters a and b mark the peaks/troughs in Stage-I and Stage-II. Calcite layers indicated by dark blue bars are marked in green in the ABC-1  $\delta^{18}\text{O}$  record. (For interpretation of the references to color in this figure legend, the reader is referred to the Web version of this article.)

## 11. 古强度结果偏差修正 (BiCEP)：一个提高的方法 对于获得古强度结果



翻译人：张伟杰 12031188@mail.sustech.edu.cn

Cych B J, Morzfeld M, Tauxe L. *Bias Corrected Estimation of Paleointensity (BiCEP): An improved methodology for obtaining paleointensity estimates*[J]. *Geochemistry, Geophysics, Geosystems*, 2021, e2021GC009755.

<https://doi.org/10.1029/2021GC009755>

**摘要：**许多天然和考古材料违反了古强度实验的假设条件，导致 Arai 图呈现出不是线性的特点，得出不准确的古强度结果，导致古强度评估的偏差。最近，古地磁学家采用了一套“选择标准”，将具有非线性 Arai 的样本排除在分析之外，但古地磁学界对使用哪一套标准几乎没有共识。在本研究中，我们提出一种统计方法：古强度结果偏差修正 (BiCEP)，本方法假设每个样本记录的古强度偏离真实结果的程度取决于一个非线性度量（曲率参数 $\vec{k}$ ）。我们可以利用这种经验关系来估计一个样本 $\vec{k}=0$ （指示此处是完美的直线）处代表的古强度。我们将 BiCEP 方法应用于 30 个原始地磁场真实值受到良好约束的采样点。我们的方法获得了古强度的准确估计，具有与严格的古强度选择标准相似的准确度和精确度水平，但是更加宽松的选择标准接受了更多采点。BiCEP 方法比使用这些选择标准具有显著的优势，因为它在不排除大量样本的情况下获得了准确的结果。它从样本均不符合传统标准的采点中得到了尽管不精确但是较为准确的估计值。BiCEP 具有最严格选择标准的准确性和不太可靠的“松散”标准的低失败率的特点。

**ABSTRACT:** The assumptions of paleointensity experiments are violated in many natural and archeological materials, leading to Arai plots which do not appear linear and yield inaccurate paleointensity estimates, leading to bias in the result. Recently, paleomagnetists have adopted sets of “selection criteria” that exclude specimens with nonlinear Arai plots from the analysis, but there is little consensus in the paleomagnetic community on which set to use. In this study, we present a statistical method we call Bias Corrected Estimation of Paleointensity (BiCEP), which assumes that the paleointensity recorded by each specimen is biased away from a true answer by an amount that is dependent a single metric of nonlinearity (the curvature parameter  $\vec{k}$ ) on the Arai plot. We can

use this empirical relationship to estimate the recorded paleointensity for a specimen where  $\vec{k}=0$ , that is, a perfectly straight line. We apply the BiCEP method to a collection of 30 sites for which the true value of the original field is well constrained. Our method returns accurate estimates of paleointensity, with similar levels of accuracy and precision to restrictive sets of paleointensity criteria, but accepting as many sites as permissive criteria. The BiCEP method has a significant advantage over using these selection criteria because it achieves these accurate results without excluding large numbers of specimens from the analysis. It yields accurate, albeit imprecise estimates from sites whose specimens all fail traditional criteria. BiCEP combines the accuracy of the strictest selection criteria with the low failure rates of the less reliable “loose” criteria.

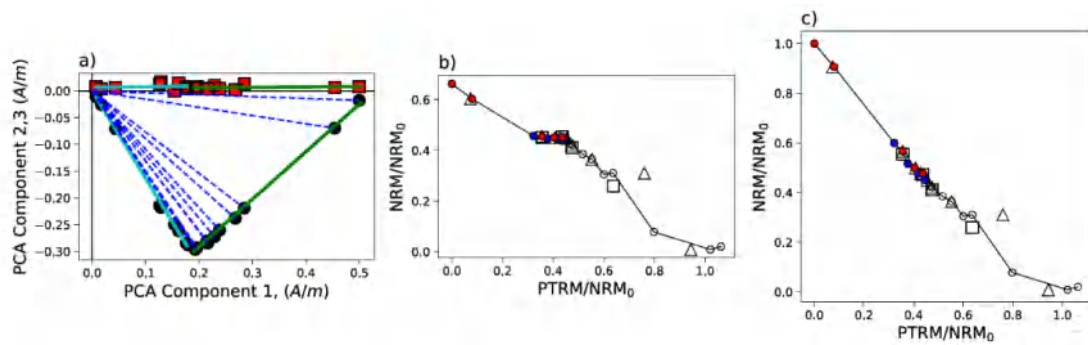


**Figure 1.** (a) Example of vector endpoint diagram for specimen FB2-B1 from Lisé-Pronovost et al. (2020). The magnetization is rotated so that the principal component of the TRM direction for all steps lies along the x axis. Green line fit to the low temperature component and cyan line fit to the high temperature component. (b) Arai plot and (c) “corrected” Arai plot for a specimen from the data shown in (b). NRM values for the low temperature component (filled circles) are usually calculated by taking the magnitude of the vector endpoint (blue dashed lines in the vector endpoint diagram in a). In (c), these NRM values are calculated by vector subtracting the high temperature component (cyan line), taking the magnitude of our new NRM vectors (distance along green line), and adding the magnitude of the low temperature component (length of cyan line). Both (b) and (c) are scaled by the total NRM distance along both components (total distance along both green and cyan lines).

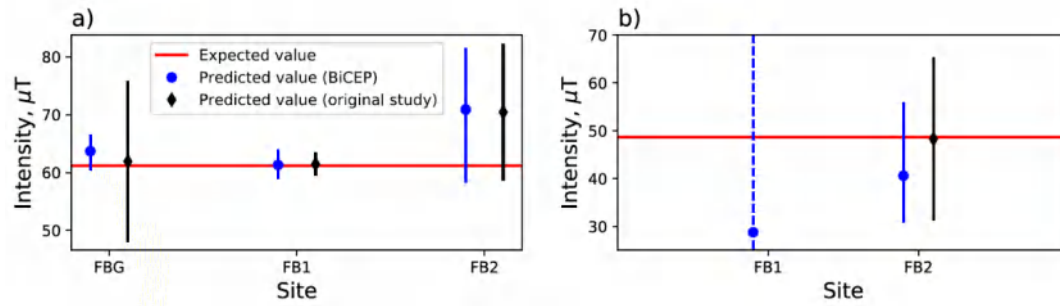


**Figure 2.** Expected and predicted intensities on the data of Lisé-Pronovost et al. (2020) using Bias Corrected Estimation of Paleointensity (blue circles) and the method used in the original study (black diamonds). (a) Results for the low temperature component (Australia, expected field value 61.17 T) for each firebrick. (b) Results for the high temperature component (Scotland, expected field value 48.3 T), where this component was present. The dashed blue line indicates that the MCMC sampler failed to converge for site FB1.

## 12. 间冰期结束时，由辐射量引发的大西洋环流突然减弱



翻译人: 张亚南 zhangyn3@mail.sustech.edu.cn

*Yin Q. Z, Wu Z. P, Berger A, et al. Insolation triggered abrupt weakening of Atlantic circulation at the end of interglacials[J]. Science, 2021,373(6558), 1035-1040.*

<https://doi.org/10.1126/science.abg1737>

**摘要:**在许多古气候记录中都可以观察到间冰期结束时的突然变冷,但其成因机制尚不清楚。通过模拟,作者认为在天文学上引起的太阳辐射量变化存在一个阈值,在过去 80 万年的间冰期结束时低于这个阈值,就会引起气候的突变。当太阳辐射量减少到临界值,就会触发持续数千年的大西洋径向翻转流(AMOC)的突然减弱和高振幅变化的冷气候状态。该机制与北欧和拉布拉多海域的海冰反馈有关。这种阈值存在的普遍性说明其在终止间冰期结束时温暖气候条件发挥着重要的作用。

**ABSTRACT:** Abrupt cooling is observed at the end of interglacials in many paleoclimate records, but the mechanism responsible remains unclear. Using model simulations, we demonstrate that there exists a threshold in the level of astronomically induced insolation below which abrupt changes at the end of interglacials of the past 800,000 years occur. When decreasing insolation reaches the critical value, it triggers a strong, abrupt weakening of the Atlantic meridional overturning circulation and a cooler mean climate state accompanied by high-amplitude variations lasting for several thousand years. The mechanism involves sea ice feedbacks in the Nordic and Labrador Seas. The ubiquity of this threshold suggests its fundamental role in terminating the warm climate conditions at the end of interglacials.

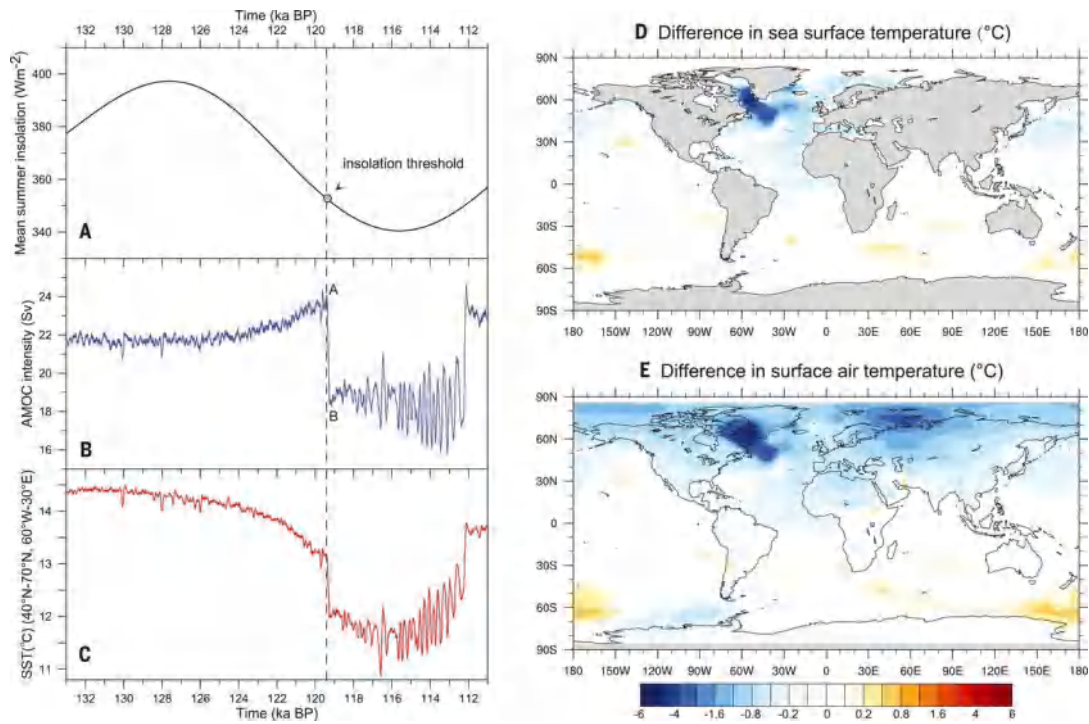


**Figure 1.** Insolation-only induced variations in AMOC and temperature during MIS-5e. (A) Mean summer insolation averaged over the four latitudes 55°N, 65°N, 75°N, and 85°N (23); the mean insolation of the half-year NH astronomical summer is obtained by dividing the total irradiation received during the half-year summer (24) by the length of the half-year summer (25). (B and C) AMOC intensity (B) and annual mean SST (C) in the North Atlantic region. (D) Difference in annual mean SST between points “B” and “A.” (E) Difference in annual surface air temperature between points “B” and “A.” The results are from the simulation with only insolation varying and CO<sub>2</sub> fixed at 280 ppmv. A 100-year running mean is applied on the simulated AMOC and SST.

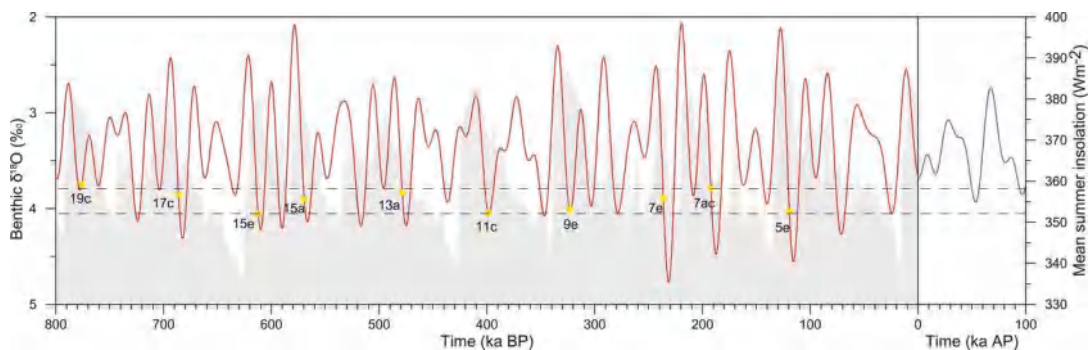


**Figure 2.** Insolation threshold band through the past 800 ka and the future 100 ka. Red and blue curves are the mean summer insolation as defined in Fig. 1. Gray shaded curve is the benthic  $\delta^{18}\text{O}$  at site U1385 (5) showing the glacial-interglacial cycles. The two horizontal dashed lines define the upper and lower

insolation threshold values  $358.2$  and  $352.1 \text{ Wm}^{-2}$ , respectively, determined from the insolation-only simulations. Yellow dots indicate the times at the end of the interglacials when abrupt weakening of AMOC is triggered.

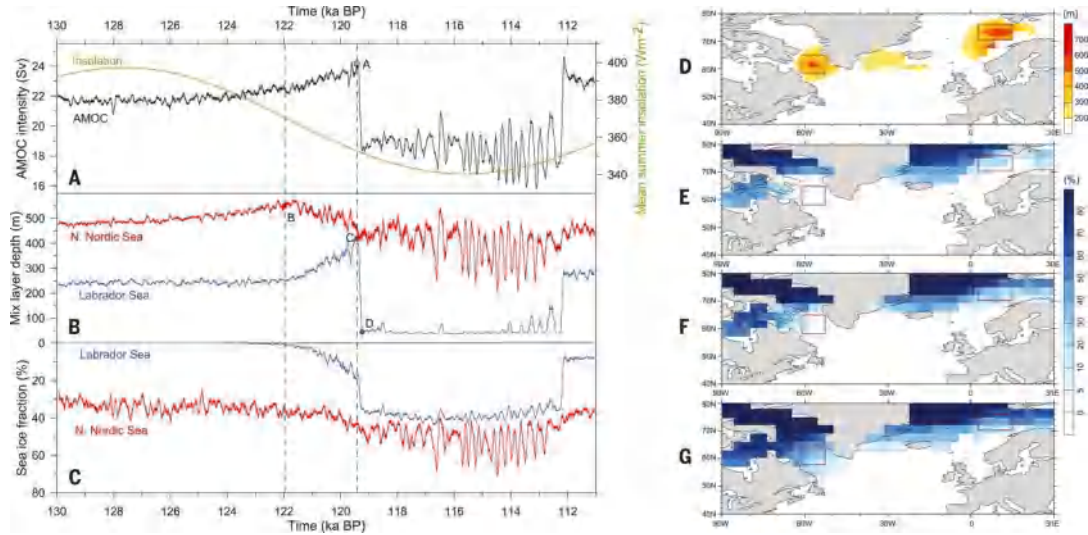


**Figure 3.** Insolation-only induced variations in AMOC, the convection and sea ice in northern Nordic Sea and Labrador Sea during MIS-5e. (A) Mean summer insolation averaged over  $55^{\circ}\text{N}$ ,  $65^{\circ}\text{N}$ ,  $75^{\circ}\text{N}$ , and  $85^{\circ}\text{N}$  (green) and AMOC intensity (black). (B) Mix layer depth in the northern Nordic Sea ( $70^{\circ}\text{N}$  to  $78^{\circ}\text{N}$ ,  $2.5^{\circ}\text{E}$  to  $17.5^{\circ}\text{E}$ ) (red) and the Labrador Sea ( $56^{\circ}\text{N}$  to  $66^{\circ}\text{N}$ ,  $62^{\circ}\text{W}$  to  $52^{\circ}\text{W}$ ) (blue). (C) Sea ice fraction in the northern Nordic Sea (red) and the Labrador Sea (blue). (D) Mix layer depth (m) at time “A.” (E), (F), and (G), Sea ice fraction at time “B,” “C,” and “D,” respectively. A 100-year running mean is applied on the simulated results. The two rectangles in (D) to (G) indicate the convection center in the Labrador Sea and the northern Nordic Sea.